Powering of endoscopic cutting tools for minimally invasive procedures

A Thesis
submitted to the faculty of the

Worcester Polytechnic Institute

as a partial fulfillment of the requirements for the
Degree of Master of Science
in
Mechanical Engineering

By

_____
Kehui Chen
28 May 2013

Approved:

_____
Prof. Cosme Furlong, Major Advisor

_____
Prof. Ryszard J. Pryputniewicz, Member, Thesis Committee

_____
Prof. Maria Chierichetti, Member, Thesis Committee

_____
Jeffery B. Ryan Jr, Interscope, Inc., Whitinsville, MA, Member, Thesis Committee

_____
Prof. Simon W. Evans, Graduate Committee Representative

Abstract

Sample cutting is an important minimally invasive medical procedure. Currently there are several types of medical devices used to cut a distal biological sample, for example, a video endoscope and TurboHawk Plaque Excision Systems.

Directional Atherectomy (DA) with the TurboHawk Plaque Excision Systems is a catheter-based, minimally invasive treatment method for peripheral arterial disease (PAD). During a procedure, a catheter is directed toward an area of plaque buildup to remove the plaque from the body, restoring blood flow (Covidien, 2013).

Endoscopy is an important procedure used in the medical field to study and diagnose different parts of a body without the need to undergo a major surgery. The major devices are a video endoscope with a flexible or rigid insertion tube and endoscopic therapy devices. Arrays of the devices, through the instrument channel in the insertion tube of endoscopes, to perform a variety of functions are offered. The biological sample cut is one of the important endoscopic therapies.

Both of Directional Atherectomy and endoscopy procedures require a power transmission from the proximal tip of device to the distal end, where the cutter is located, for cutting a sample. However, the working length is up to meters, and the diameter of the devices is in millimeter scale in the minimally invasive surgery. Thus enough power transmitting to the distal end of the device for the biological sample cutting is crucial.

This research presents the effort toward the investigation of the potential power

mechanisms from the proximal tip to the cutter at the distal end of the device for rapid rotational cutting motion to improve the cutting efficiency and accuracy.

In this thesis, the potential powering mechanisms including fluid, electrical, and torque coils are investigated.

Since the transmission power is used for a rotational cutting action, and the cutting geometry has influence on the cutting power, thus this research also focuses on the analysis of the cutting geometry for the rotational sample cutting. The Hertz contact theory and von Mises yield criterion are used to find the influence of tool geometry on the material removing process, as well as Abaqus, a commercial FEM software, is used for the finite element analysis. Fiber-reinforced composite structures are the main characteristic of the representative biological sample, and their mechanical behavior is strongly influenced by the concentration and structural arrangement of constitute such as collagen and elastin. Researches show that the biological sample, for example, a soft biological sample, has hyperelastic properties and behave anisotropically, and there are a few publications about the plastic properties and cutting mechanics. Thus a linear elastic and linear plastic material model is defined for the finite element analysis of material removal. The analytical results and finite element results both show that as the tool rake angle increases or the tool angle decreases, the magnitude of cutting force decreases.

A preliminary representative sample cutting experiment was conducted, and standard

cutters with different cutting geometries were tested in order to find the characteristic of the biological sample cutting and the influence of tool geometry on the required cutting power. The experiments reveal the same conclusions as the analytical and finite element results.

***Keywords*:** Abaqus, contact stress, cutting geometry, minimally invasive surgery, sample cutting, von Mises yield criterion

Acknowledgments

I would like to thank my advisor Professor Cosme Furlong for giving me the opportunity to do my thesis on such an exciting area of research and for the guidance he has provided along the way. The project would not have made it as far as it did without the help of all the members of the Center for Holographic Studies and Laser micro-Mechatronics. I would like to particularly appreciate Interscope sponsoring me during this project.

Accolades are also extended to Babak Seyed Aghazadeh, Caoyang Ti, Zhibo Cao, Ellery Harrington, Ivo Dobrev, Morteza Khaleghi Meybodi, Weina Lu, Peter Hefti, Xiaoran Chen, and Weiyuan Tie from the CHSLT laboratories for their enduring support and invaluable assistance.

Finally, I want to thank my dear family for their love and unending support throughout my tenure. Without them I would not have been able to accomplish anything.

Table of contents

List of figures

List of tables

Nomenclature

DA	Directional Atherectomy
PAD	Peripheral arterial disease
$h_{friction}$	Head loss in a pipe flow
$\sum h_{local}$	Energy loss due to channel bends in a pipe flow
$\rho_1,\ \rho_2$	Fluid density at location 1 and location 2 in a pipe flow, respectively
$z_1,\ z_2$	Distances between location 1 and location 2 to the ground, respectively
$p_1,\ p_2$	Fluid static pressures at location 1 and location 2 in a pipe flow, respectively
f	Channel friction factor
D	Pipe inner diameter
Q	Fluid flow rate in pipe
Re	Reynolds number
ν	Fluid kinematic viscosity
E_0	Induced voltage in the armature in a motor
Z	Total number of conductors in armature of a motor
Φ	Magnetic flux per pole in a motor

N	Rotation speed of a motor
B	Magnetic material's magnetic induction
l	Length of a rotor in a motor
r	Radius of a rotor in a motor
E_s	Source voltage of a motor
R_a	Armature resistance of a motor
ρ	Electrical resistivity of copper in a motor
L	Total length of copper wire in a motor
LED	Light-emitting diode
CCD	Charged coupled device
PVC	Polyvinyl chloride
σ_θ	Hoop stress in cylindrical polar coordinates
σ_r	Radial stress in cylindrical polar coordinates
σ_z	Axial stress in cylindrical polar coordinates
p_m	Contact mean pressure in sphere contacts plate problem
a	Contact radius in contact problem
p_0	Maximum contact pressure in sphere contacts plate problem
E	Young's modulus
υ	Possion's ratio in contact problem

$A_{project}$	Projected contact area in contact problem
V	Velocity of the material in orthogonal cutting model
ϕ_0	Shear angle in orthogonal cutting model
α_0	Rake angle in orthogonal cutting model
τ	Friction angle in orthogonal cutting model
μ	Friction coefficient between cutting tool and material in orthogonal cutting model
β	Cutting tool angle in orthogonal cutting model
γ	Clearance angle in orthogonal cutting model
$\{f\}$	Vector of displacement at any point of the element in FEM
$\{N\}$	Matrix of shape functions in FEM
$\{\delta\}^e$	Vector of nodal displacements at any point of the element in FEM
$\{\varepsilon\}$	Vector of strain at any point of the element in FEM
$[B]$	Strain-displacement matrix in FEM
$\{\sigma\}$	Vector of stress at any point of the element in FEM
$[D]$	Elastic matrix related to the material elastic properties in FEM
$[k]^e$	Element stiffness matrix in FEM
$[k]$	Structure stiffness matrix in FEM

$[F]$	Force vector in FEM
$[\delta]$	Nodal displacement vector of all elements in FEM
ω	Damage parameter in element failure model in Abaqus
$\bar{\varepsilon}^{pl}$	Initial value of the equivalent plastic strain in element failure model in Abaqus
$\Delta\bar{\varepsilon}^{pl}$	An increment of the equivalent plastic strain in element failure model in Abaqus
$\bar{\varepsilon}_f^{pl}$	Strain at failure in element failure model in Abaqus
A	A point on the deforming mesh of specimen in element failure model in Abaqus
X_A	The current coordinate of point A on the deforming mesh of specimen in element failure model in Abaqus
C	A point in the cutting tool in element failure model in Abaqus
X_C	The current coordinate of point C on the deforming mesh of specimen in element failure model in Abaqus
A'	Closest point on the surface of the cutting tool to point A
$\vec{n}$	Normal vector from point A' to point A
$\vec{r}$	Vector from point C to point A'
h	Distance between point A and point A'

c	Clearance below which contact occurs
t_α	Tangents to the surface at point $A^{'}$
$\overrightarrow{S^\alpha}$	Measure distance along t_α to the surface at point $A^{'}$
$\delta\gamma_\alpha$	'Slip' of point $A^{'}$
$\dot{h}$	Velocity term
$\ddot{h}$	Acceleration terms
RP	Reference point
Δt	Stable time increment in FEM
$\omega_{\max}$	Highest frequency of the system in FEM
L^e	Element length in FEM
c^d	Wave speed of the material in FEM
CPS4R	A 4-node bilinear plane stress quadrilateral, reduced integration, hourglass control element type

Objectives

Sample cutting is an important minimally invasive medical procedure. Since the working length of the current devices, for example, the video endoscope and the TurboHawk system, is up to meters, and the diameter is in millimeter-scale, achieving enough cutting power for rotational cutting at the distal end of the devices is a challenge. Our research presents the effort toward the investigation of the feasibility of potential power mechanisms from the proximal tip to the cutter at the distal end of the devices for a rotational cutting motion to improve the cutting efficiency and accuracy. In this thesis, the potential powering mechanisms including fluid, electrical, and mechanical mechanisms are investigated.

In addition, the cutting geometries are analyzed due to the influence on the rotational cutting performance such as cutting power.

1. Introduction

Sample cutting is an important minimally invasive procedure. In this Chapter, the current devices are introduced. In addition, current common characteristic and challenge of the distal biological sample cutting are presented for aid in determining the need of the investigation of the powering mechanisms for the rotational cutting at the distal end of the devices for rapid and accurate sample cutting to perform minimally invasive surgical procedures.

1.1 Directional atherectomy with TurboHawk system

The TurboHawk System is a directional atherectomy platform to safely treat peripheral arterial disease (PAD) above and below the knee (Covidien, 2013). The TurboHawk system contains a flexible drive shaft, a control handle, and a cutter at the distal end of the flexible drive shaft, which is shown in Fig. 1.1.

Fig. 1.1. TurboHawk System (Covidien, 2013).

The cutter at the distal end of the flexible drive shaft, as shown in Fig. 1.2 (a), is used to cut the sample. An access device, such as a guidewire or a sheath, is placed in the target vessel. Then the TurboHawk device approaches the plaque burden in vessel along the access device. When the cutter contacts the sample, it starts to rotate and moves forward by the control of the proximal tip of the flexible shaft, which is shown in Fig. 1.2 (b).

(a)

(b)

Fig. 1.2. (a) A four contoured blades cutter at the distal end of the flexible drive shaft in TurboHawk System (Covidien, 2013); (b) Sample removal using the cutter at the distal end of the flexible drive shaft in TurboHawk System (Covidien, 2013).

The rotational cutting action or cutting power is transmitted from the proximal end of the flexible drive shaft to the cutter at the distal end of the flexible shaft. The working length of the TurboHawk system is up to meter, the diameter is in millimeter scale, which are shown in Table 1.1.

Table 1.1. Geometry information of the TurboHawk System (Covidien, 2013).

	Catalog Number	Vessel Diameter (mm)	Crossing Profile (mm)	Working Length (mm)	Effective Length (mm)	Max. Cut Length (mm)
LARGE VESSEL	THS-LS-C	3.5-7.0	2.7	1100	1040	50
	THS-LX-C			1300		75
	TH-LS-M			1100		50
	TH-LX-M			1130		75
SMAL VESSEL	THS-SX-C	2.0-4.0	2.2	1350	1290	40
	THS-SS-C			1330		20
	THS-SS-CL			1490	1450	20
	P4028	1.5-2.0	1.9	1350	1320	10

1.2 Endoscopic sample cutting

1.2.1 Endoscopy and endoscopes

In recent years, endoscopy becomes an increasingly important medical therapy for studying and diagnosing different parts of a body without the need to undergo a major surgery. The primary devices used in an endoscopy procedure are a video endoscope with a flexible or rigid insertion tube and endoscopic devices, which are shown in Fig. 1.3 and Fig. 1.4.

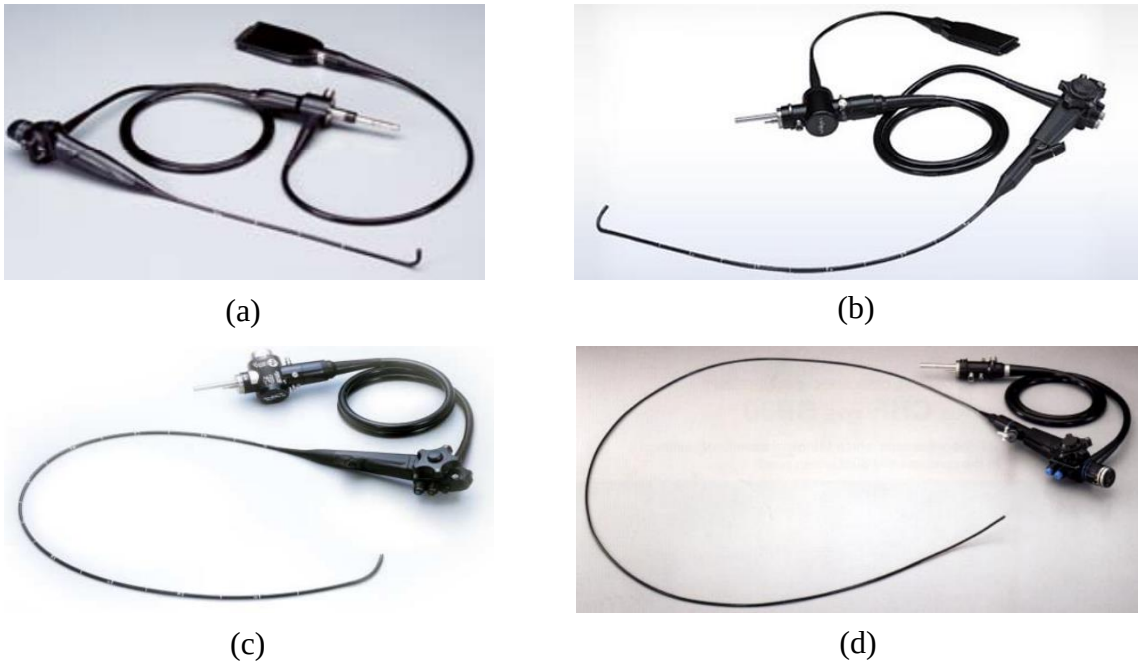

(a) (b)

(c) (d)

Fig. 1.3. Four types of video endoscopes: (a) a rhinolaryngoscope model ENF-VQ: 3.6 mm diameter flexible insertion tube with 3.9 mm diameter distal end (Olympus, 2013); (b) an esophagoscope model PEF-V: 5.3 mm diameter flexible insertion tube with 2.0 mm instrument channel and working length of 650mm (Olympus, 2013); (c) a gastroscopes model GIF-N180: 4.9 mm diameter flexible insertion tube with 2.0 mm diameter instrument channel and total working length of 1100 mm (Olympus, 2013); (d) a choledochoscope model CHF-BP30: 3.4 mm diameter flexible insertion tube with 1.2mm instrument channel and total working length of 1870 mm (Olympus, 2013).

(a)

(b)

(c)

(d)

Fig. 1.4. Endoscopic devices: (a) grasping forceps (Foreign body retrieval, 2013), (b) hemostatic clips (Hemostasis Products, 2013), (c) biopsy forceps (EndoJaw, 2013), (d) aspiration needle (EZ Shot2, 2013).

An endoscope is a major diagnostic, therapeutic, and screening tool used to view inside the body by inserting the flexible or rigid insertion tube into a natural or created aperture in the body without the need to make a major surgical incision. The crucial component of endoscopes is the insertion tube, which may be rigid or flexible. The important internal components in insertion tube include the water channel, air channel, light guide, objective lens or eyepiece, and biopsy or instrument channel as shown in Fig. 1.5.

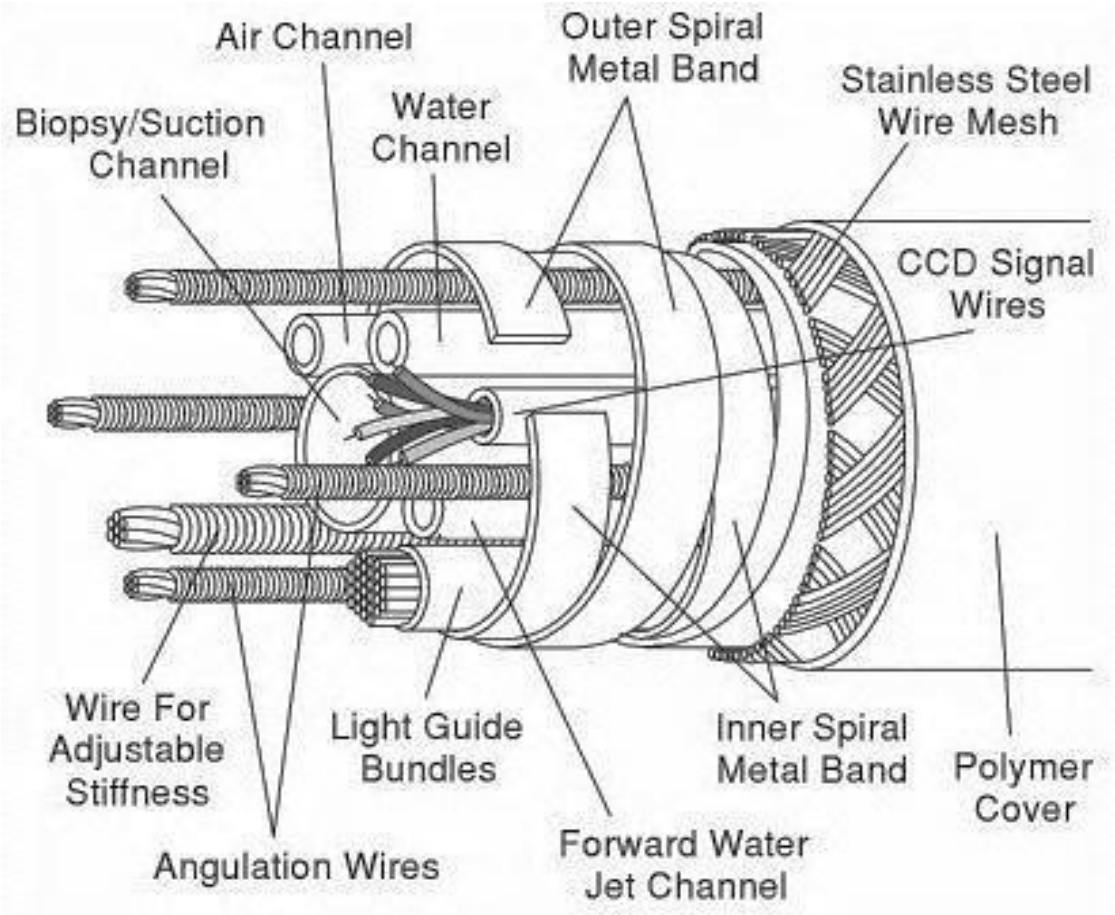

Fig. 1.5. Internal components and construction in a flexible insertion tube of a video endoscope: water channel, air channel, biopsy/suction channel, CCD signal wires, and light guide bundles (Cotton, 2008).

During the endoscope procedure, the endoscopic devices pass through the biopsy/suction channel or instrument channel arriving at the target position for surgery. Currently, there are a wide range of endoscopes used for different portions of the body, which include gastroscope, rhinolaryngoscope, and so on. The types and detailed information of endoscopes are shown in Table 1.2 (Olympus, 2013; Pentax, 2013; Fujinon, 2013). The maximum insertion tube diameter is 13.3 mm, and the instrument

channel diameter varies from 0.75 mm to 6.0 mm. The working length is from 250mm to 2180 mm. Figure 1.6 shows a distal end of a video endoscope with instrument channel.

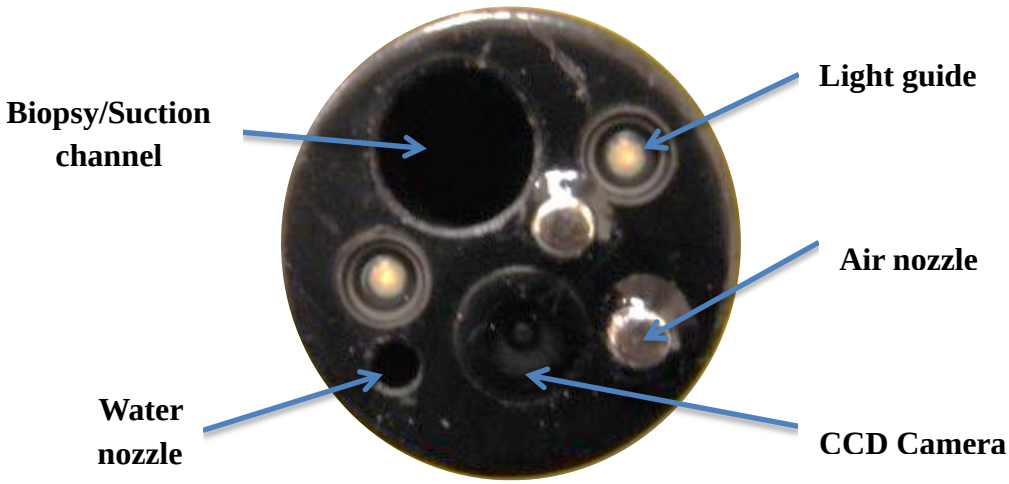

Fig. 1.6. The distal end of a video endoscope including light guide, biopsy/suction channel, water nozzle, air nozzle and CCD camera.

Table 1.2. Types of endoscopes.

Name	Application tissue	Field of View (degree)	Insertion tube diameter (mm)	Instrument channel diameter (mm)	Working length (mm)	Tip Deflection (degree)
Rhinolaryngoscope	**Nose and throat**	**75/85/90**	**1.8-4.9**	**--/2**	**270-635**	**Up/Down 130**
Larynogoscope	**Throat**	**90**	**3.0-5.2**	**1.2-3.0**	**600**	**Up/Down 120**
Gastroscope	**Stomach**	**120/140**	**5.1-12.8**	**2.0-6.0**	**925-1100**	**Up 210 Down 90 Right 100 Left 100**
Bronchoscope	**Bronchial tubes**	**80 /120**	**3.8-7.0**	**1.2-3.6**	**550-840**	**Up 120-180 Down 90-130**
Choledochoscope	**Bile duct**	**90/125 air 83water**	**2.8-4.9**	**0.75-2.2**	**900-1870**	**Up 160 Down 130**
Duodenoscope	**Designed for ERCP**	**A side view: 90/100**	**7.4-12.6**	**2.0-4.8**	**250-1030**	**Up 120 Down90 Left 90 Right 110**
Enteroscope	**Duodenum**	**140**	**5.0-13.2**	**1.0-3.5**	**800-2180**	**Up/Down 180 Right/Left 160**
Sigmoidoscope	**Rectum and sigmoid colon**	**120/140**	**12.2-13.3**	**3.2-4.2**	**630-790**	**Up/Down 180 Right/Left 160**
Colonoscope	**Colon**	**140/170**	**12.8-13.2**	**3.2-4.2**	**700-2180**	**Up/Down 180 Right/Left 160**

1.2.2 Endoscopic devices for sample cutting

The biopsy forceps or aspiration needles are used for sample cutting, which pass through the instrument channel of endoscopes. The transmission length of the sample cutting action from the proximal tip of the endoscopic device to the removal tools at the distal end is up to meters, and the crossing profile is in millimeter scale.

1.2.2.1 Biopsy forceps

A biopsy forceps is an endoscopic devices used for sample cutting or acquisition. One type of biopsy forceps is shown in Fig. 1.7 (a), which includes a control handle, a flexible tube, and a cutting tip at the end of the flexible tube. The working principle of the biopsy forceps is:

1. Biopsy forceps pass through the instrument channel and arrives at the target area, as shown in Fig. 1.7 (b).
2. The cutting tip of biopsy forceps at the distal end of the flexible tube approaches to the target, which is shown in Fig. 1.7 (c).
3. The cutting tip is cutting the target sample by pulling the control handle at the proximal tip of the flexible tube, as shown in Fig. 1.7 (d).
4. The sample is collected by the biopsy forceps as shown in Fig. 1.7 (e).

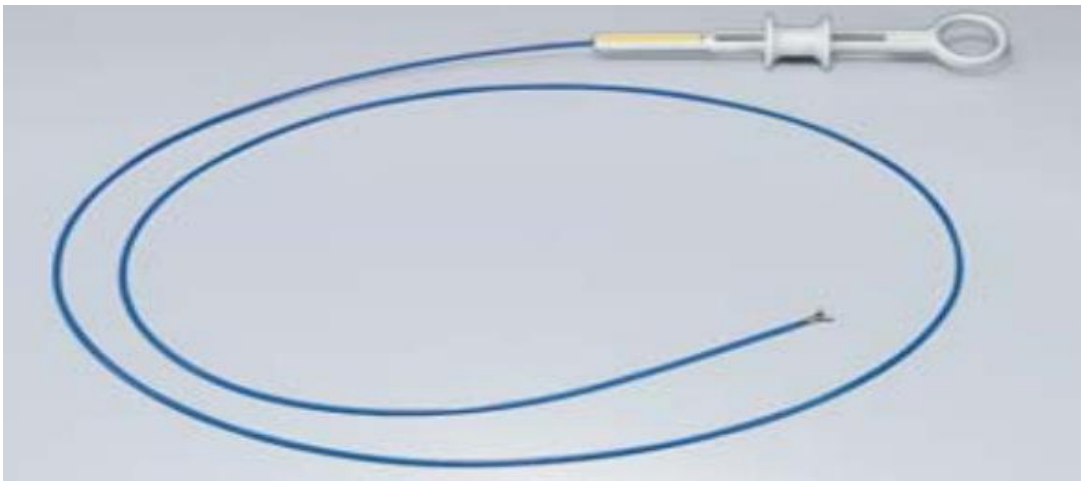

(a)

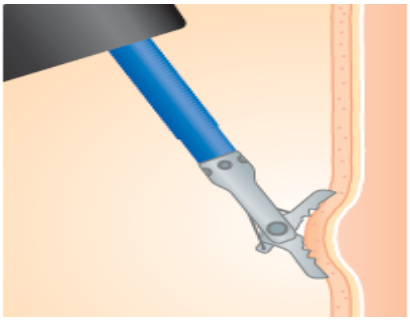

(b)

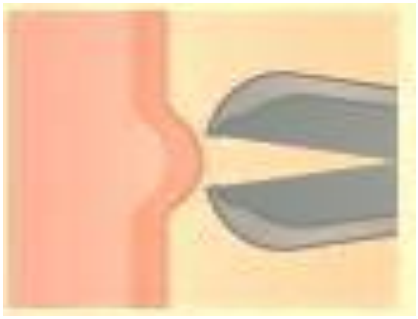

(c)

(d)

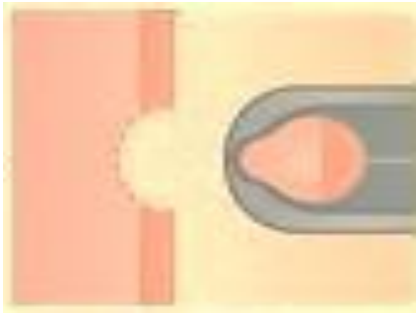

(e)

Fig. 1.7. Biopsy forceps and the working principle of biopsy forceps: (a) biopsy forceps with a control handle, a flexible tube, and a cutting tip; (b) biopsy forceps inserted into endoscope instrument channel and arriving at target area; (c) biopsy forceps approaching to the target area; (d) biopsy forceps cutting sample; (e) biopsy forceps collecting sample (EndoJaw, 2013).

1.2.2.2 Aspiration needles and cytology brushes

An aspiration needle is utilized in ultrasonic endoscopes for sample collection and thinner brushes are used for specimen collection in pulmonary diagnosis (Olympus, 2013). The needle and brush are shown in Fig. 1.8. The needle or brushes are inserted through the instrument channel by pushing control handles and when the tools arrive at the target area the samples are removed by aspiration or abrasion.

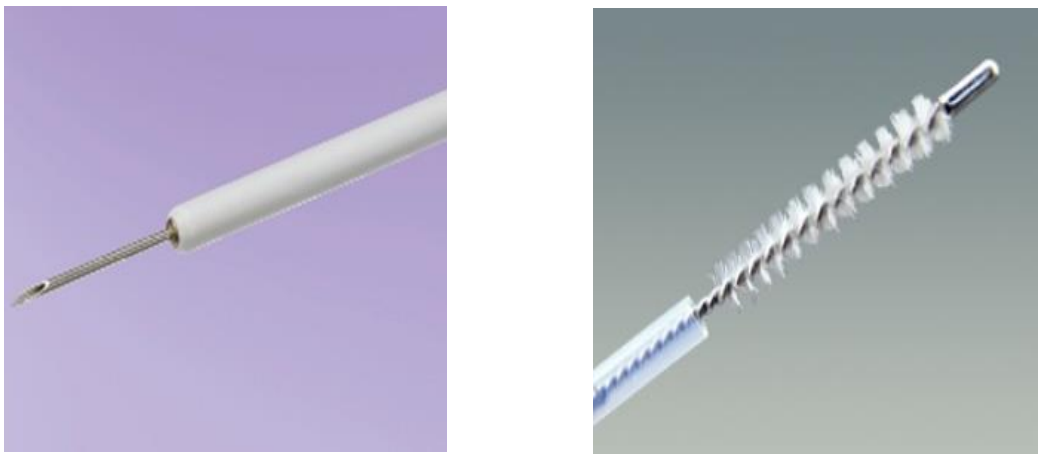

(a) (b)

Fig. 1.8. (a) Aspiration needle; (b) Cytology brushes (Enteroscopy, 2013).

1.3 Common characteristics and challenges

Minimally invasive surgery is a procedure by inserting the devices into a natural or created tiny aperture in the body instead of a major surgical incision to perform a surgery. Sample cutting is an important minimally invasive medical treatment. In recent years, some medical devices, for example, an endoscope or TurboHawk system, are used for

removing sample without undergoing a major surgery (Covidien, 2013).

The characteristic of current devices are long and slim due to the insertion of the devices to a tiny aperture for performing a minimally invasive surgery inside of body. The working length of the TurboHawk system is from 1100 mm to 1450mm, and the diameter is from 1.9 mm to 2.7 mm. The length of the endoscopes working channel, which allows the endoscopic devices, for example, biopsy forceps, to pass through, is up to 2180 mm, and the diameter is from 0.75 mm to 6.0 mm.

The sample cutting at the distal end of the devices is achieved by the power or cutting action transmission from the proximal tip to the distal end of the devices. Thus, for a biological sample cutting during a minimally invasive surgery, the transmission of the power or a cutting action from the proximal tip of the removal devices to the cutter at the distal end is required. However, the big challenge of the sample cutting is how to transmit enough power or the cutting action from the proximal end to the distal tip of the devices through a long and slim channel or shaft. Thus, an investigation of potential powering mechanisms is conducted.

2. Potential powering mechanisms

The goal of this project is to investigate the potential power mechanism for a rotational cutting action at the distal end of medical devices in a minimal invasive surgery to achieve a highly efficient cutting performance. This can facilitate the sample cutting by decreasing removing time in the whole procedure and to improve the accuracy of the therapy.

Since the diameter of the medical devices is in millimeter scale, and the working length is up to meters, one of the difficulties of the project is enough power transmitting from the proximal tip to the devices at the distal end for continuous rotational cutting. In this Section, the potential power mechanisms are investigated and evaluated including fluid, electrical and torque coils. The rotational cutting torque for a representative biological sample cutting is in Newton millimeter scale at the distal end of the devices, whose diameter is in millimeter scale (Chanthasopeephan et al., 2003).

2.1 Fluid-compressed air/water

Compressed air/water is a popular method of the power supply to medical devices, which is inexpensive, clean and contains no toxicity. In addition, based on the research by the Richard Dennis National Energy Technology Laboratory in Fossil Energy program at U.S. Department of Energy, the efficiency of gas turbine mechanism is up to 60% (Richard Dennis National Energy Technology Laboratory, 1992). The efficiency of

some water turbines such as Francis turbine is up to 90% (Water turbine, 2013). Thus, a turbine mechanism powered by gas or water can be a potential mechanism. However, the working length of the sample cutting devices is a challenge in the long-distance flow transmission. When air or water flows in the transmission channel, the energy losses due to the friction caused by shear stresses along channel walls, $h_{friction}$ and local losses, $\sum h_{local}$, that arises at channel bends, valves, enlargements, contractions, etc., which is shown in Fig. 2.1.

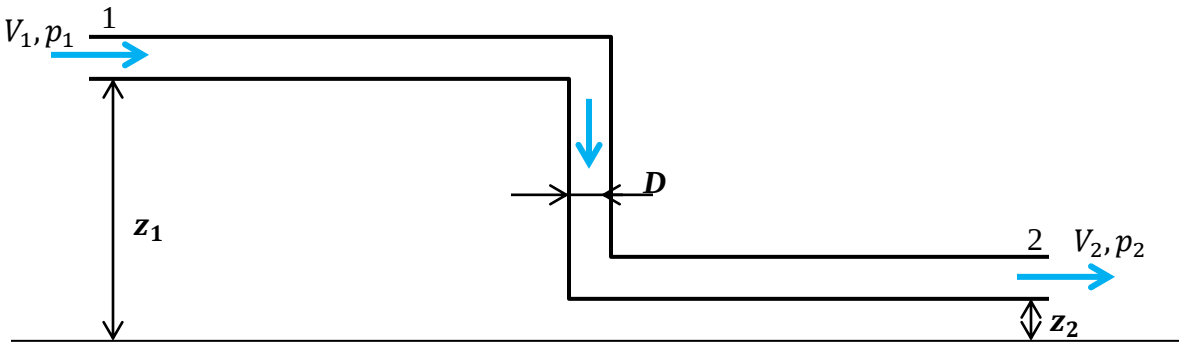

Fig. 2.1. Fluid flow in a bent tube, the energy losses due to the friction caused by shear stress along tube walls and the local losses that arises at tube bends and contractions.

The energy equation is (Fay, 1998):

$$\frac{p_1}{\rho_1 g} + z_1 + \frac{V_1^2}{2g} = \frac{p_2}{\rho_2 g} + z_2 + \frac{V_2^2}{2g} + \sum h_{losses}, \tag{2.1}$$

$$\sum h_{losses} = h_{friciton} + \sum h_{local}, \tag{2.2}$$

where ρ_1 and ρ_2 are the fluid density at location 1 and 2, respectively. z_1 and z_2 are the distances between location 1 and location 2 to the ground, respectively. p_1 and

p_2 are the fluid static pressures at location 1 and location 2, respectively. V_1 and V_2 are the fluid velocities at location 1 and location 2, respectively.

In a straight pipe, the term of local lost $\sum h_{local}$ can be eliminated.

The energy losses due to friction $h_{friction}$ can be calculated by Darcy-Weisbach equation (Fay, 1998)

$$h_{friction} = f \frac{8L}{D^5} \frac{Q^2}{g\pi^2}, \tag{2.3}$$

where f is the pipe friction factor and D is the pipe diameter in meter. Q is the flow rate in pipe.

The pipe friction factor is related to the Reynolds number Re for laminar flow and is given by the following formula (Fay, 1998):

$$f = \frac{64}{\mathrm{Re}}, \tag{2.4}$$

where $\mathrm{Re} = \frac{4Q}{\pi D \nu}$, which is the Reynolds number. ν is the fluid kinematic viscosity.

Assuming one straight pipe is used for fluid transfer and $z_1 = z_2 = 0$, and the pipe diameter $D = 1.0mm$. The flow is incompressible and the density of water is $\rho_1 = \rho_2 = 1000kg/m^3$. In addition, the fluid velocity at point 1 is $2m/s$ and according to the continuity equation, the velocity at point 2 is the same as at point 1. The fluid kinematic viscosity is $\nu = 10^{-6} m^2/s$. The total pressure at point 1 including static and dynamic pressure is 40 psi. The turbine at the power portion of the device is located at point 2, thus the ratio of energy lost due to friction to the total energy along the pipe

length is shown in Fig. 2.2.

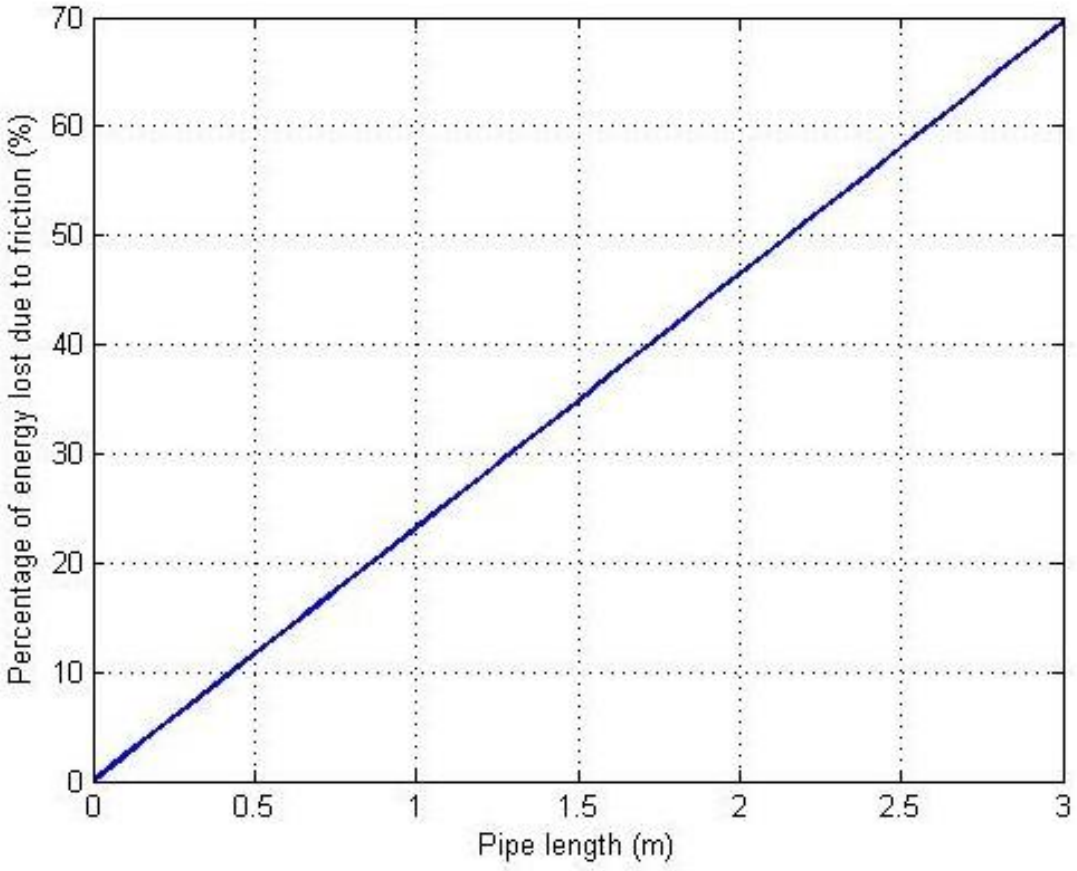

Fig. 2.2. Energy lost due to friction to the total energy along the pipe length.

Therefore, in obtaining a specific value for powering the turbine located at the distal end of the sample cutting devices, the energy lost increases as the transmission length increases. In this case, the energy lost is up to 70%, when the transmission length is up to 3.0 m.

In addition, there are bent sections of the transmission channel during the procedure, thus the energy lost is much higher than the calculated result.

2.2 Electrical

In recent years, the use of mini or micro motors is increasing significantly in the medical devices due to the advantages of accurate control, and researches focus on the application of micro motors for minimal invasive surgery (Gao et al., 1998).

The power generated by a permanent magnet DC motor is given by the following formulation (Wildi, 2005):

$$P = E_0 \times I \,, \tag{2.5}$$

where E_0 is the induced voltage in the armature and I is the total current supplied to the armature.

$$E_0 = Z\Phi N / 60 \,, \tag{2.6}$$

$$\Phi = ZBlr \cos\left(\frac{\pi Nt}{30}\right), \tag{2.7}$$

where Z is the total number of conductors in armature. Φ is the magnetic flux per pole in Weber. N is the rotation speed in rpm and B is the magnetic material's magnetic induction in T. l is the length of the rotor, and r is the rotor radius.

$$I = (E_s - E_0) / R_a \,, \tag{2.8}$$

where E_s is the source voltage in Volts, and R_a is the armature resistance

$$R_a = \rho \frac{L}{s} \,, \tag{2.9}$$

where ρ is the electrical resistivity of copper. The constant value is $1.724 \times 10^{-8} \Omega \cdot m$. L is the total length of copper wire, and s is the cross-section area of copper wire.

However, the electrical motor is needed to be integrated with the sample cutting devices, whose working length is up to meters, and the diameter is in millimeter scale. The flexible shaft of the devices give the bent capability when it is inside organs or vessels, whereas the tip of the cutting is rigid. The maximum length of rigid distal tip of endoscope is 15 mm (Olympus, 2013; Pentax, 2013; Fujinon, 2013). Thus, the length of electric motor should be smaller than the length of the rigid tip. The largest outer diameter of DC motor should be less than the diameter of the transmission channel, and the output torque is in Newton millimeter scale at a rotation speed for the representative biological sample cutting. A micro motor based on an endoscope is developed (Gao et al., 1998). The performance data of the electromagnetic micro motor is shown in Table 2.1. However, the produced torque is too small. Recently, there are several commercial companies in the world developing the micro DC motors whose diameter is from 2.0 mm to 4.0 mm with the 0.5 mm or 0.8 mm shafts.

Table 2.1. Performance data of the electromagnetic micro motor (Gao et al., 1998).

Diameter of rotor	Overall size	Speed	Torque	Current
2 mm	2 mm	3000 rpm	1.5 μNm	120 mA

Currently, the output torque of a commercial DC motors with 4.0 mm outer diameter by Namiki is $70\mu Nm$ at rotation speed 3000 rpm. The length is over 15.0 mm and the

shaft diameter is 0.5 mm. Thus the output torque of the micro motors, whose diameter is smaller than 4.0 mm, and the length is smaller than 15mm, is in micro Newton-meter scale. Moreover, the cost of electrical motor is relatively high compared with other methods.

2.3 Mechanical mechanism- torque coil

Torque coil is a flexible solid or hollow metal tube with multiple layers and multiple threads. The function of torque coil is similar to a flexible shaft, which can transmit the rotation of the proximal end accurately to the distal tip. The distinctive advantage of the torque coil is that can transmit the rotation even if there are some bent sections. The structure of the torque coil is shown in Fig. 2.3.

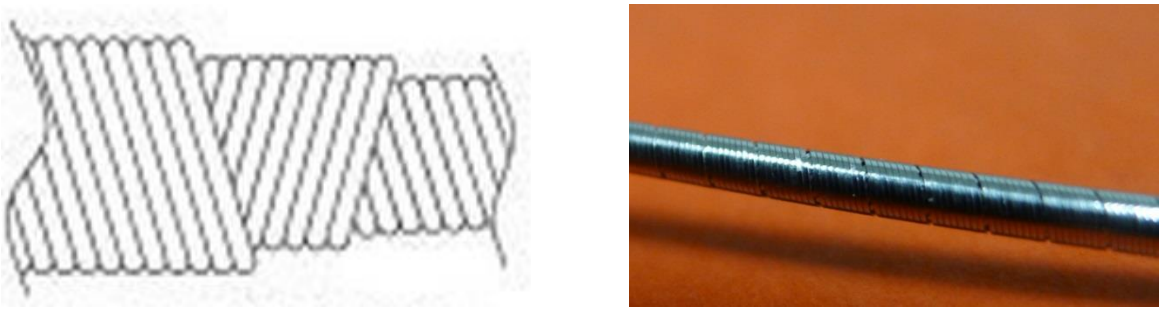

(a) (b)

Fig. 2.3. (a) Torque coil schematic drawing (ASAHI INTECC, 2013), and actual torque coil of 2.210mm outer diameter.

SS304 and SS316 are popular materials used for torque coil, both materials are

approved by FDA for medical device. Since during the sample cutting procedure the power or action transmission shaft of the devices in body is bent, the rotation transmission through the transmission shaft is nonlinear, bent and long distance, which is difficult and a challenge for a conventional rotational transmission mechanism such as a rigid shaft. However, the application of torque coils eliminates the difficulty. Besides, the multiple sizes of the torque coils give the capability of integration with different sample cutting devices. Table 2.2 shows two types of hollow torque coils supplied by ASAHI INTECC.

Table 2.2. Major dimensions of the torque coil samples (ASAHI INTECC, 2013).

Sample	O.D. (mm)	I.D. (mm)	Material	Layer	Length(mm)
Sample 1	1.950	1.420	SS304	1	2470.0
Sample 2	2.210	1.500	SS304	2	1955.0

Based on the information supplied by the manufacturer (ASAHI INTECC, 2013), the accuracy of the rotational transmission between the proximal end and the distal tip is up to 1:1, which means the rotation transmission is very accurate. However, there is no information about the maximum rotation speed of the torque coil. A torque coil rotation speed monitor system is set up, which is shown in Fig. 2.4. The proximal end of torque coil is connected to an electrical motor. The distal tip of torque coil is connected to a

rigid shaft, which is exposed by a LED light. The LED controller is connected to the function generator. The function generator sends a pulse signal to the LED controller, thus the LED light is acting as a strobe light, and the frequency of the strobe light is adjusted by the frequency of the pulse signal. When the frequency of the strobe light is equal to the frequency of the rotation of the distal tip of torque coil, the rotation is 'frozen', which is captured by CCD camera, and the rotation speed is obtained. The rest of torque coil is within a PVC tube. The inner diameter of the PVC tube is 2.33 mm.

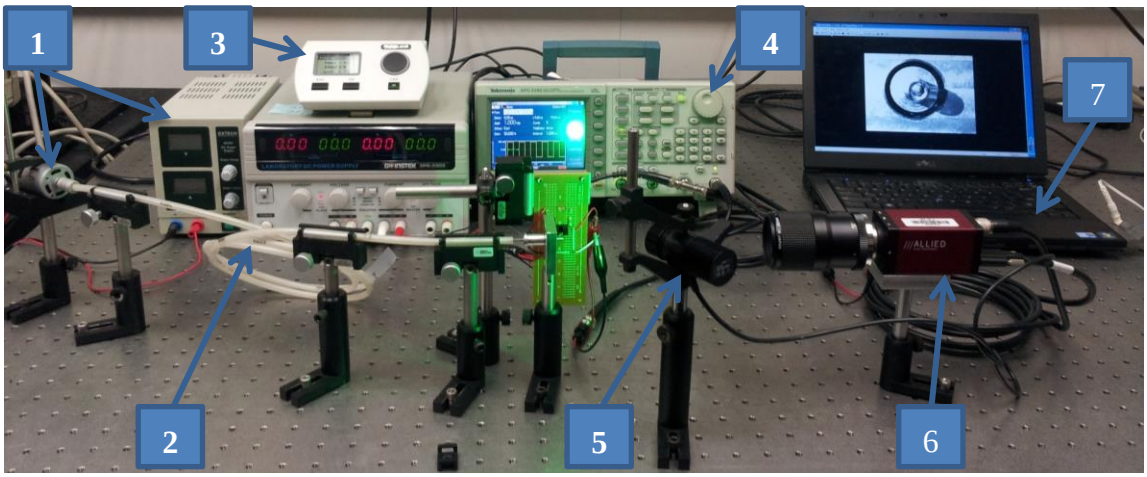

Fig. 2.4. Torque coil rotation speed measurement system: 1 are DC motor and DC motor power supplier; 2 is the torque coil within PVC tube; 3 is LED controller; 4 is function generator; 5 is LED; 6 is CCD camera;7 is PC.

The tests run at low rotation speed around 400 rpm and high rotation speed 1400 rpm. The 'frozen' images are captured when the rotation speed are around 400 rpm, which are shown in Fig. 2.5. Two samples are tested and the experimental results are shown in Fig. 2.6 and Fig. 2.7.

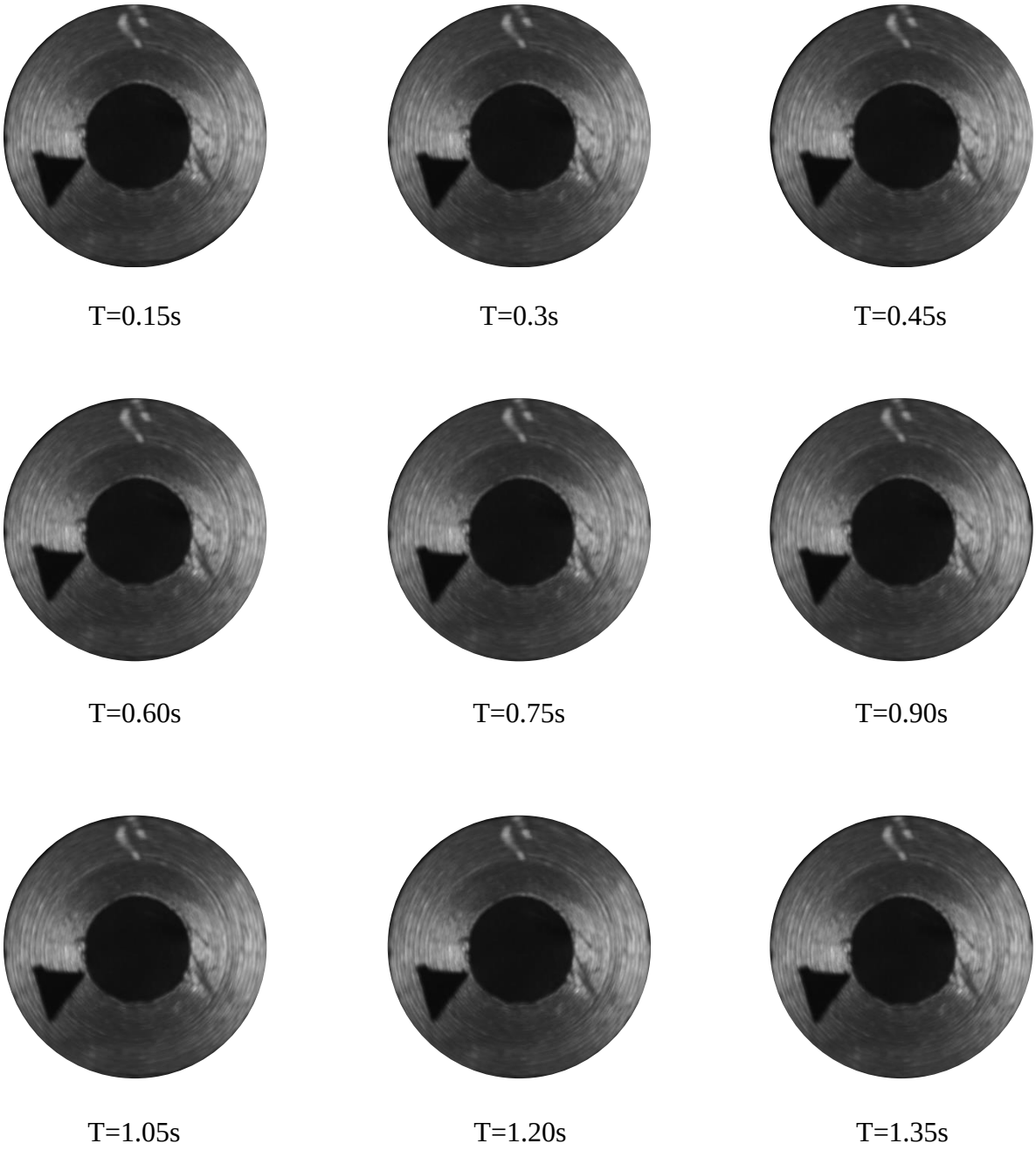

Fig. 2.5. Representative images of the distal tip of torque coil rotating at speed of 400 rpm captured by the camera in time interval of 0.15s. The capture time period is determined by the strobe light frequency. When the strobe light frequency is equal to the frequency of torque coil rotation, the captured images are the same, which is "frozen".

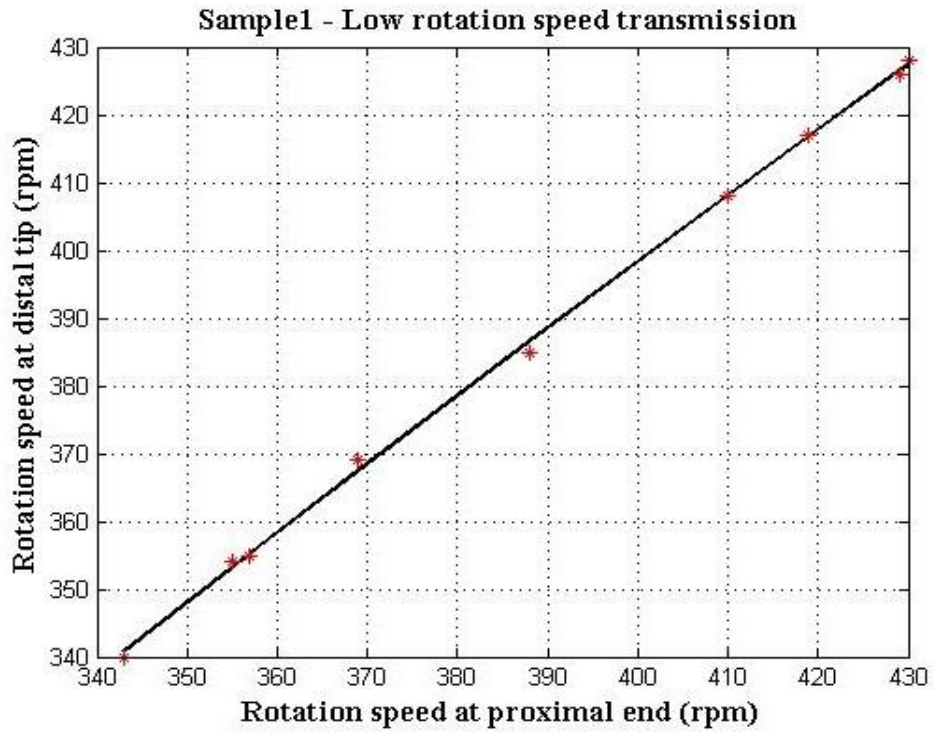

(a)

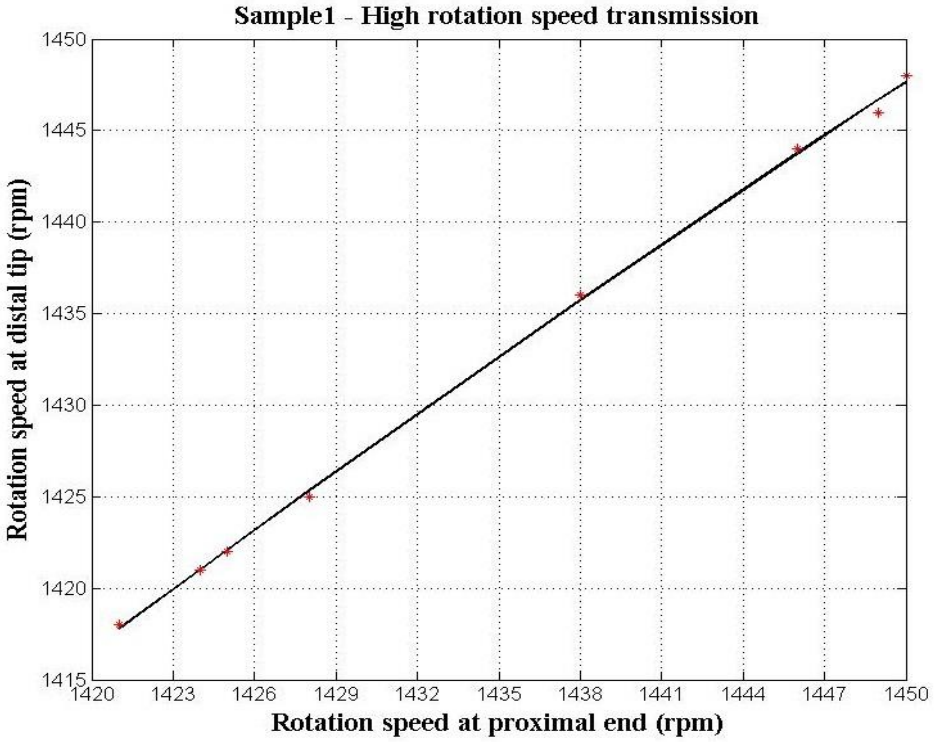

(b)

Fig. 2.6. Different rotational speed tests for finding the maximum rotation speed of sample 1: (a) low rotation speed test, (b) high rotational speed test.

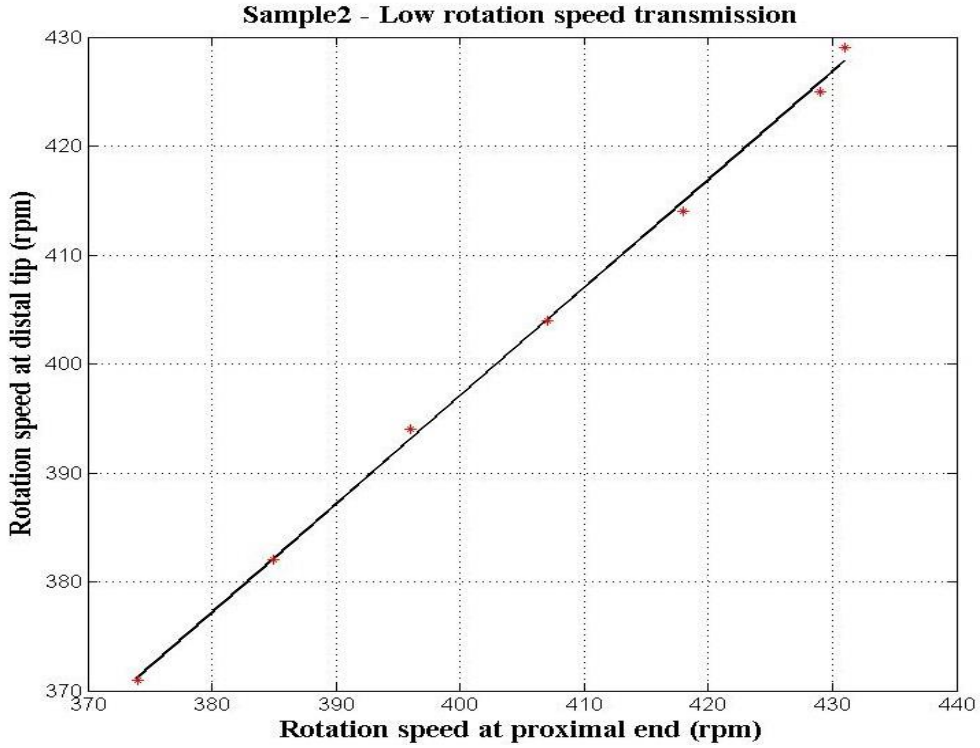

(a)

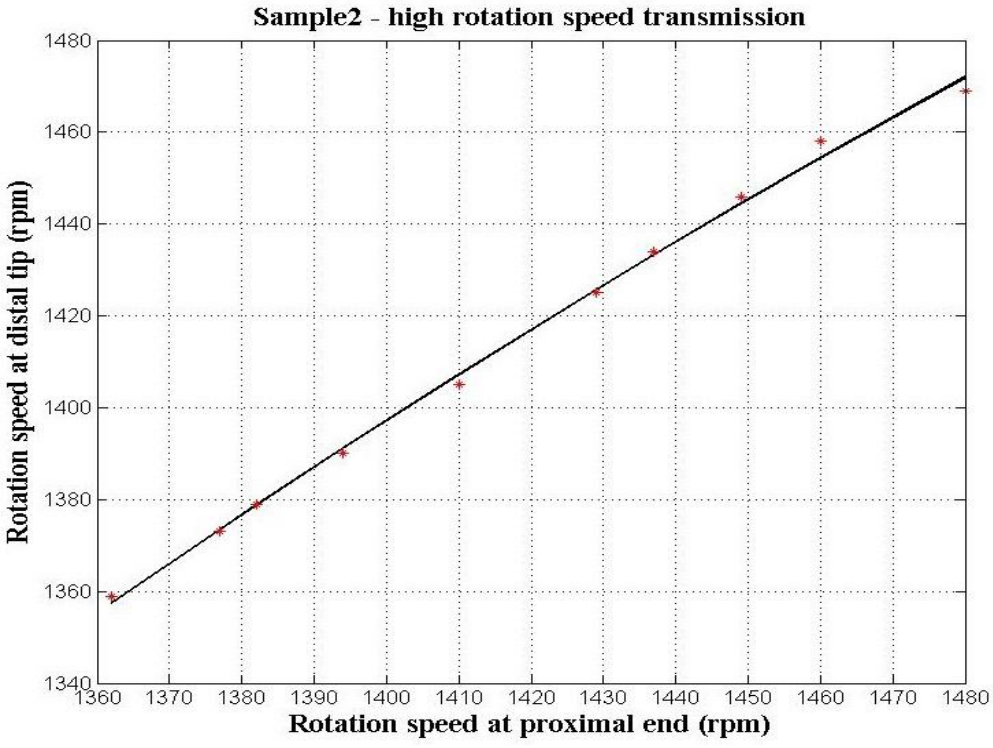

(b)

Fig. 2.7. Different rotational speed tests for finding the maximum rotation speed of sample 2: (a) low rotation speed test, (b) high rotational speed test.

From the experimental results, the rotation transmission is stable and uniform. No delay or significant vibration is at the distal tip of the torque coil. In addition, the rotation transmission is nearly linear. However, when the torque coil runs at rotation speed of above 1400 rpm, there is a fluctuation, which may be explained that there is some plastic deformation or torsion on the torque coil caused by the friction.

As the rotation speed increasing, the plastic deformation increases, and finally the torque coils are failed at around 1800 rpm after 5 mins running. Fig. 2.8 illustrates the failure of the torque coil tested in the system shown in Fig. 2.4. The failure location is at the connection with the motor.

Fig. 2.8. Torque coil failed during the rotation test shown in Fig. 2.4. The failure occurs at the connection with the motor.

Thus, the accuracy of the rotation transmission of torque coil is up to 1:1, which supplies a capability of an accurate rotation transmission from the proximal end to the distal tip. However, when the torque coil rotates at high speed, there will be some

torsion or failure, which should be taken into account when the high rotation speed transmission is required.

3. Mechanics of cutting

The thesis focuses on the investigation of the power mechanisms for rapid rotational cutting action in millimeter scale. Since the cutting geometry has influence on the required cutting force or power, in this Section the theory of contact mechanics and orthogonal cutting mechanics are used to find the relationship between the tool geometry and the cutting force or power.

Based on the contact mechanics, the shapes of contact objects influence the stress distribution and the location of first yield. Thus, the contact of a rigid sphere and a deformable flat surface, as well as a rigid cone and a deformable flat surface are investigated respectively in this Section in order to find the stress distribution under the surface, and where the first yield occurs under the same pure normal load, which will be a benefit to determine the cutting geometry.

3.1 Introduction

The cutting process is also the material elastic and plastic deformation, fracture and removal process. There are three regions of material response to the compression of cutting tool (Fischer-Cripps, 2007), which is shown in Fig. 3.1.

1. Region1 - Full elastic response, no permanent or residual impression left in the test specimen after removal of load
2. Region2 - Plastic deformation exists but is constrained by the surrounding elastic

material

3. Region3- Plastic region extends and continues to grow in size and fracture or failure occurs.

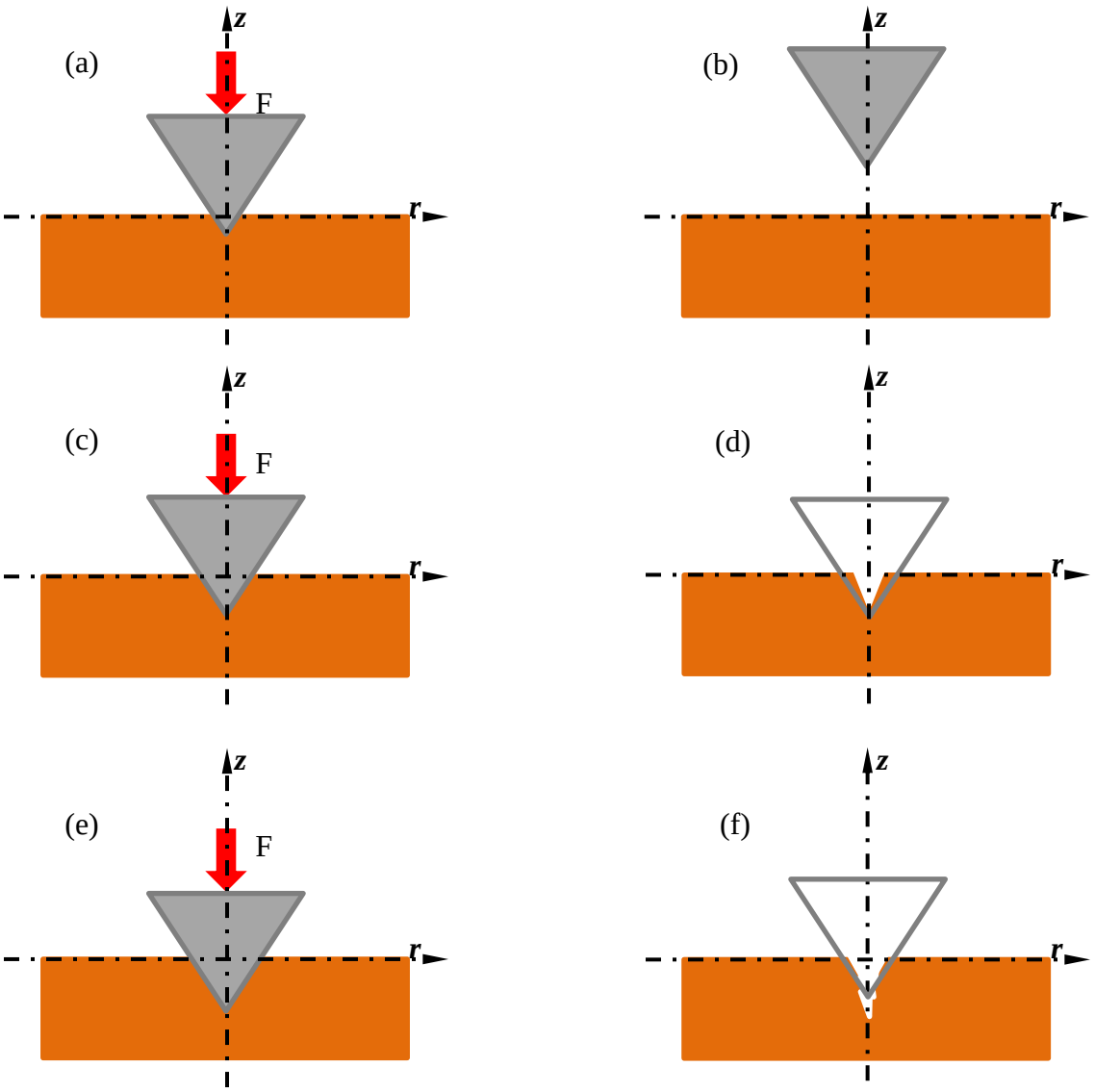

Fig. 3.1. A deformable plate responds to a normal load applied by a rigid cone: (a) a normal load is applied, there is elastic deformation in the plate; (b) if the load is removed, the deformation of plate recovers due to the elastic deformation; (c) the increment of the load and contact lead the deformation to increase; (d) the plastic and elastic deformation occur; if the load is removed, there is some elastic recovery; (e) the increment of the load and contact lead to the plastic deformation increase and fracture occur; (f) there is fracture occurring on the plate.

In the Region 1, during the initial application of load, the response is elastic and can be predicted from the Hertz relation (Hertz, 1881).

Hertz contact problem is the study of contact between two continuous, non-conforming solids. The contact between these two solids is initially a point or line. The sphere and cone contact with the flat surface are introduced.

3.2 Axial symmetrical elastic analysis

In three dimensional contact problems, the axial symmetrical elastic analysis can be simplified greatly by conversion to cylindrical polar coordinates (r,θ,z). In the contact problem, the hoop stress σ_θ is always a principal stress, because of the symmetry within the stress field. σ_r, σ_z and σ_θ are independent of θ, and $\tau_{r\theta}=\tau_{\theta z}=0$. In the contact problem, it is convenient to calculate the principal stress in the *rz* plane by the following equations (Fischer-Cripps, 2007):

$$\sigma_{1,3}=\frac{\sigma_r+\sigma_z}{2}\pm\sqrt{\left(\frac{\sigma_r-\sigma_z}{2}\right)^2+{\tau_{rz}}^2}\,, \tag{3.1}$$

$$\sigma_2=\sigma_\theta\,, \tag{3.2}$$

$$\tau_{\max}=\frac{1}{2}(\sigma_1-\sigma_3). \tag{3.3}$$

3.3 Sphere contact flat surface

The original work in contact mechanics by Hertz dates back to 1881. Hertz studied the two spheres contact problem under a normal compressive load. The amount of deformation depends on the material's Young's modulus, Poisson's ratio, and radii of the spheres, as well as the normal load. For the sphere contact the flat surface, one of the radii can be taken as infinite.

The normal pressure distribution directly beneath a sphere was (Hertz, 1881):

$$\frac{\sigma_z}{p_m} = -\frac{3}{2}\left(1-\frac{r^2}{a^2}\right)^{1/2} \qquad r \le a, \tag{3.15}$$

where p_m is the contact mean pressure. a is the contact radius, and $p_m = \frac{P}{\pi a^2}$.

Thus, at the center of contact area, there is a maximum $\sigma_z = 1.5 p_m$ and at the edge of the contact area there is a minimum $\sigma_z = 0$. Outside of the contact area is a free surface where the normal stress $\sigma_z = 0$.

The normal displacement of points on the surface in the contact area, which is measured with respect to the original specimen surface (Johnson, 2003),

$$u_z = \frac{1-\nu^2}{E}\frac{3}{2}p_m\frac{\pi}{4a}\left(2a^2 - r^2\right) \quad r \le a. \tag{3.16}$$

Within the interior of the specimen, the stresses distribution expressions (Huber, 1904; Lawn et al., 1974):

$$\frac{\sigma_r}{p_m} = \frac{3}{2}\left\{\frac{1-2\nu}{3}\frac{a^2}{r^2}\left[1-\left(\frac{z}{u^{1/2}}\right)^3\right]+\left(\frac{z}{u^{1/2}}\right)^3\frac{a^2u}{u^2+a^2u^2}+\frac{z}{u^{1/2}}\left[u\frac{1-\nu}{a^2+u}+(1+\nu)\frac{u^{1/2}}{a}\tan^{-1}\left(\frac{a}{u^{1/2}}\right)-2\right]\right\}, \tag{3.17}$$

$$\frac{\sigma_\theta}{p_m} = -\frac{3}{2}\left\{\frac{1-2\nu}{3}\frac{a^2}{r^2}\left[1-\left(\frac{z}{u^{1/2}}\right)^3\right]+\frac{z}{u^{1/2}}\left[u\frac{1-\nu}{a^2+u}-(1+\nu)\frac{u^{1/2}}{a}\tan^{-1}\left(\frac{a}{u^{1/2}}\right)+2\nu\right]\right\}, \tag{3.18}$$

$$\frac{\sigma_z}{p_m} = \frac{3}{2}\left(\frac{z}{u^{1/2}}\right)^3\left(\frac{a^2u}{u^2+a^2z^2}\right), \tag{3.19}$$

$$\frac{\tau_{rz}}{p_m} = -\frac{3}{2}\frac{rz^2}{u^2+a^2z^2}\left(\frac{au^{1/2}}{u+a^2}\right), \tag{3.20}$$

where

$$u = \frac{1}{2}\left[\left(r^2+z^2-a^2\right)+\left[\left(r^2+z^2-a^2\right)^2-4a^2z^2\right]^{1/2}\right].$$

Because this problem is an axis-symmetric problem, the principal stress in *rz* plane could be solved by the Eqs 3.1 to 3.3. The distribution of maximum shear stress and von Mises are shown in Fig. 3.2 and Fig. 3.3, respectively.

The stresses along z-axis are calculated from (Johnson, 2003):

$$\frac{\sigma_r}{p_0} = \frac{\sigma_\theta}{p_0} = -(1+\nu)\left\{1-\left(\frac{z}{a}\right)\tan^{-1}\left(\frac{a}{z}\right)\right\}+\frac{1}{2}\left(1+\frac{z^2}{a^2}\right)^{-1}, \tag{3.21}$$

$$\frac{\sigma_z}{p_0} = -\left(1+\frac{z^2}{a^2}\right)^{-1}, \tag{3.22}$$

where p_0 is the maximum contact pressure

Based on the equation 3.21 and 3.22, the stress distribution along the depth below contact area could be observed in Fig. 3.4. It is shown the maximum shear stress and von Mises located below the contact area, which means that the point of first yield is hidden beneath the surface. For Poisson's ratio $\nu = 0.3$, the location is $z = 0.49a$.

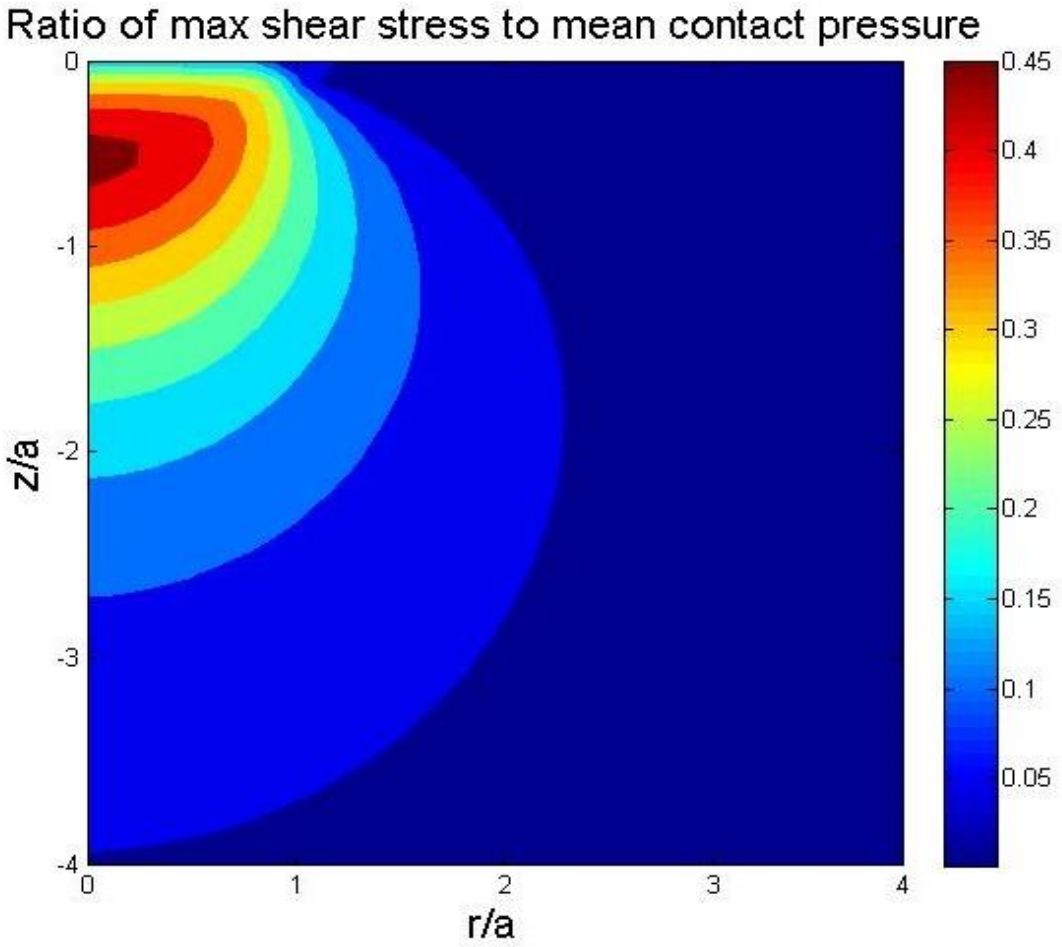

Fig. 3.2. Contour of equal maximum shear stress for spherical contact calculated for Poisson's ratio $\nu = 0.3$. Distances *r* and *z* normalized to the contact radius *a* and stresses expressed in terms of mean contact pressure.

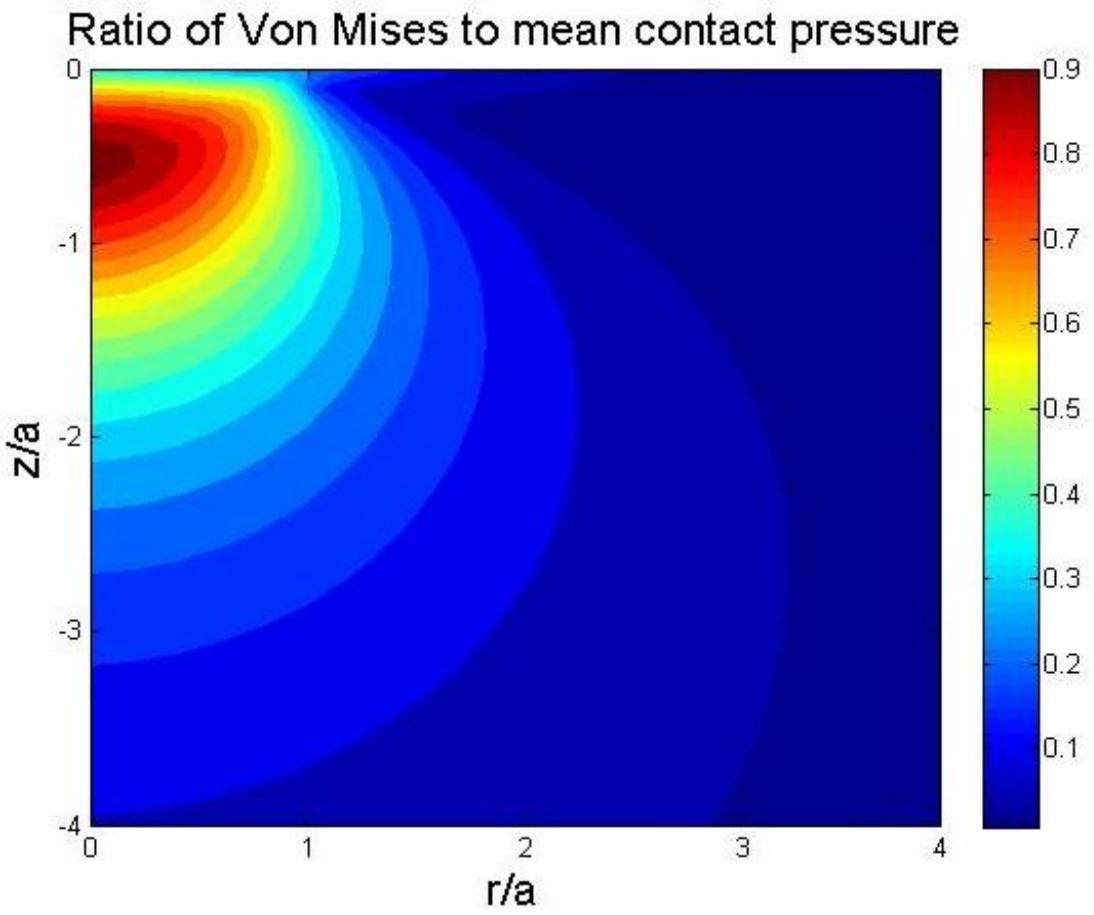

Fig. 3.3. Contour of equal von Mises stress for spherical contact calculated for Poisson's ratio $\nu = 0.3$. Distances *r* and *z* normalized to the contact radius *a* and stresses expressed in terms of mean contact pressure.

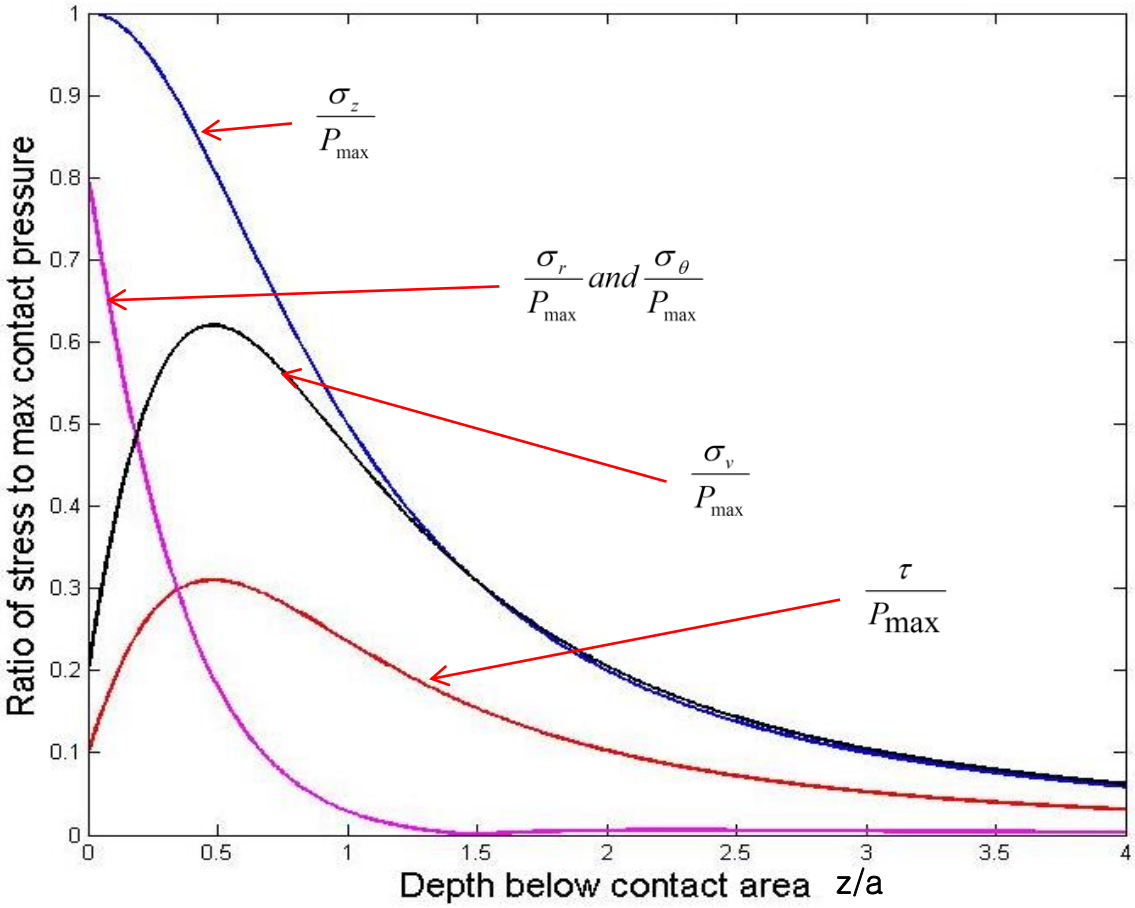

Fig. 3.4. The ratio of stress distribution to contact pressure along z-axis below the contact area of the contact between a sphere and a flat surface for Poisson's ratio $\nu = 0.3$.

3.4 Rigid cone contact surface

Rigid cone contact surface is hot practical interest because this is used for material hardness tests. The displacement of points in the contact area measured with respect to the original specimen free surface is given by (Sneddon, 1948):

$$u_z = \left(\frac{\pi}{2} - \frac{r}{a}\right) a \cot\alpha \quad r \le a\,, \tag{3.23}$$

where a is the contact radius.

The pressure distribution on the face of the cone (Johnson, 2003):

$$p_{(r)} = \frac{E}{2(1-\upsilon^2)} \cot\alpha \cosh^{-1}(a/r)\,, \tag{3.24}$$

where α is the cone semi-angle, E is the specimen Young's modulus, and υ is the specimen Possion's ratio.

Equation 3.24 shows that a theoretically infinite pressure exists at the apex. By considering the variations in stress along the z-axis, the principal shear stress (Johnson, 2003) is:

$$\tau = \frac{1}{2}\left|\sigma_r - \sigma_z\right| = \frac{E}{2\left(1-\upsilon^2\right)} a^2 \cot\alpha \left(a^2 + z^2\right)^{-1}. \tag{3.25}$$

There is a maximum yet finite value $\tau = \frac{E}{2\left(1-\upsilon^2\right)} \cot\alpha$ at the apex. In this case two principal stresses $\sigma_r = \sigma_\theta$, so that the von Mises criteria are identical if expressed in term of Y, where Y is the yield, or flow stress, of the specimen. Thus yield will

initiate at the apex if the cone angle is such that

$$\frac{E}{1-\upsilon^2}\cot\alpha \geq Y\,. \tag{3.30}$$

Thus for incompressible material, there is hydrostatic pressure combined with a finite shear at the apex.

Hence, in the Region 1 - full elastic response of the specimen, the contact pressure $p = \frac{E}{1-\upsilon^2}\cot\alpha$, depends only on the cone angle and is independent of the load. Thus the contact pressure increases with the decreasing cone semi-angle, which could explain the sharper cutting tool have a better cutting performance.

The ratio of stresses to $\frac{E}{1-\upsilon^2}$ along the z-axis when the contact radius is 1.0 mm, and the cone semi-angle is 30° is plotted in Fig. 3.5. The von Mises stress distribution with different cone semi-angle when the contact radius 1.0 mm is shown in Fig. 3.6.

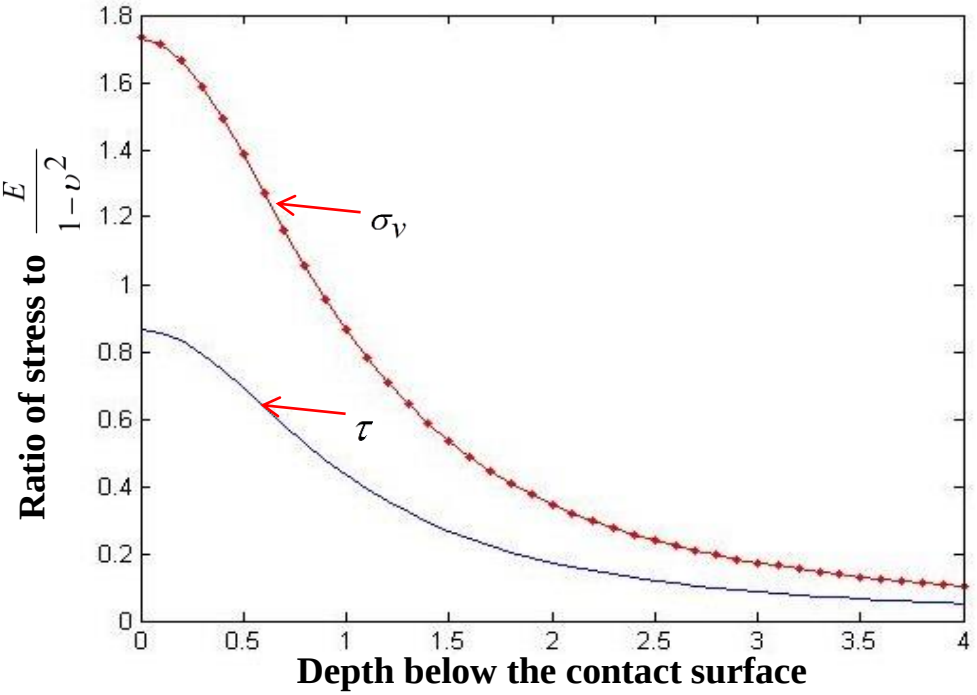

Fig. 3.5. Conical contact stress distribution along z-axis for cone semi-angle of 30°.

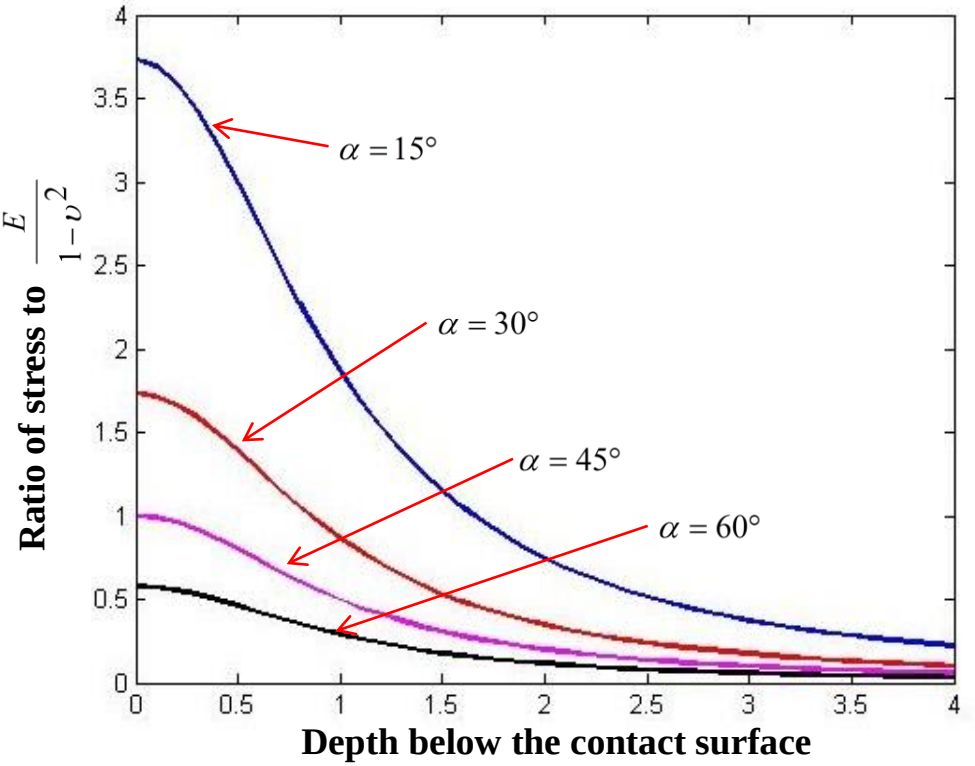

Fig. 3.6. Conical contact von Misese stress distribution of von Mises along z-axis for cone semi-angle of 15°, 30°, 45°and 60°, respectively.

However in Region 3, the plastic material is no longer elastically constrained, and the plastic strains are large compared with the elastic strains, the elastic deformation maybe neglected. Thus, it could be taken as a rigid-perfectly-plastic solid. Plastic yield in such a material depends upon a critical shear stress which may be calculated using von Mises failure criteria. In the slip-line field solution, assuming there is frictionless contact between the compression tool and specimen. The material in the region ABCDE flows upward and outward as the tool moves downward under load. Because there is no friction, the direction of stress along the line AB is normal to the face. The lines in the region ABCDE are oriented at 45° to AB and are called 'slip lines' as shown in Fig. 3.7 (Fischer-Cripps, 2007).

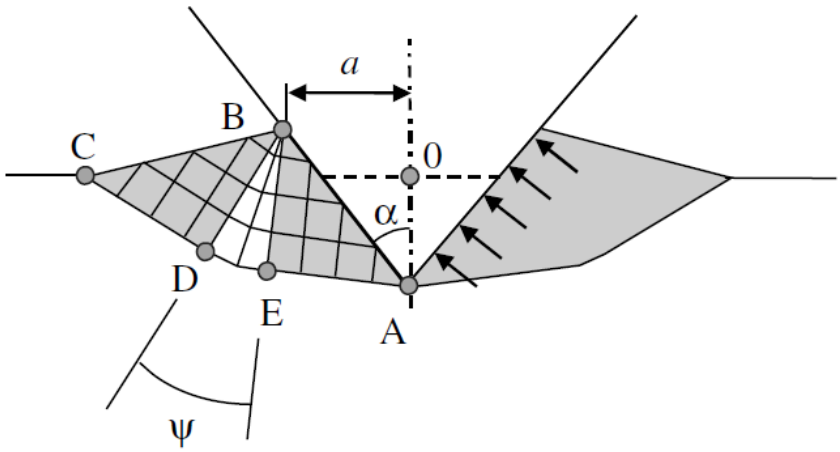

Fig. 3.7. Slip-line theory in two dimensions by Hill et al., 1947, (Fischer-Cripps, 2007).

If the tool penetrates the specimen with a constant velocity and the geometrical

similarity is maintained, the angle Ψ can be chosen so that the velocities of element of material on the free surface, contact surface, and boundary of the rigid plastic material are consistent. The contact pressure across the face of the tool is given by (Fischer-Cripps, 2007)

$$p_m = 2\tau_{\max}(1+\alpha) = Y(1+\alpha), \tag{3.31}$$

where

$$p_m = \frac{P}{A_{project}}.$$

For a conical tool, the projected area $A_{project}$ is depend of h_c and $\tan\alpha$. h_c is the depth of penetration measured from the area of contact. Thus for a certain material, as the tool semi-angle decreases, the load for cause the specimen deforming and fracturing decreases, which could explain the cutting tool geometry could affect the cutting force.

3.5 Orthogonal cutting

There are three major ways the cut geometry can be classified: orthogonal, oblique, and three dimensional cutting. Orthogonal cutting uses a single cutting edge, and the velocity of the work-piece material *V*, is orthogonal to this cut edge.

In this Section, the cutting force is analyzed based on De Vries' model, 1991, where the orthogonal cutting mechanics is employed (De Vries, 1991). Furthermore based on the knowledge of cutting operation such as tool geometry, cutting condition (i.e. depth of

cut, feed-rate, and friction angle) leads to the estimation of the cutting force that can be calculated by the following equation (De Vries, 1991). The mechanics of orthogonal cutting is shown in Fig. 3.8.

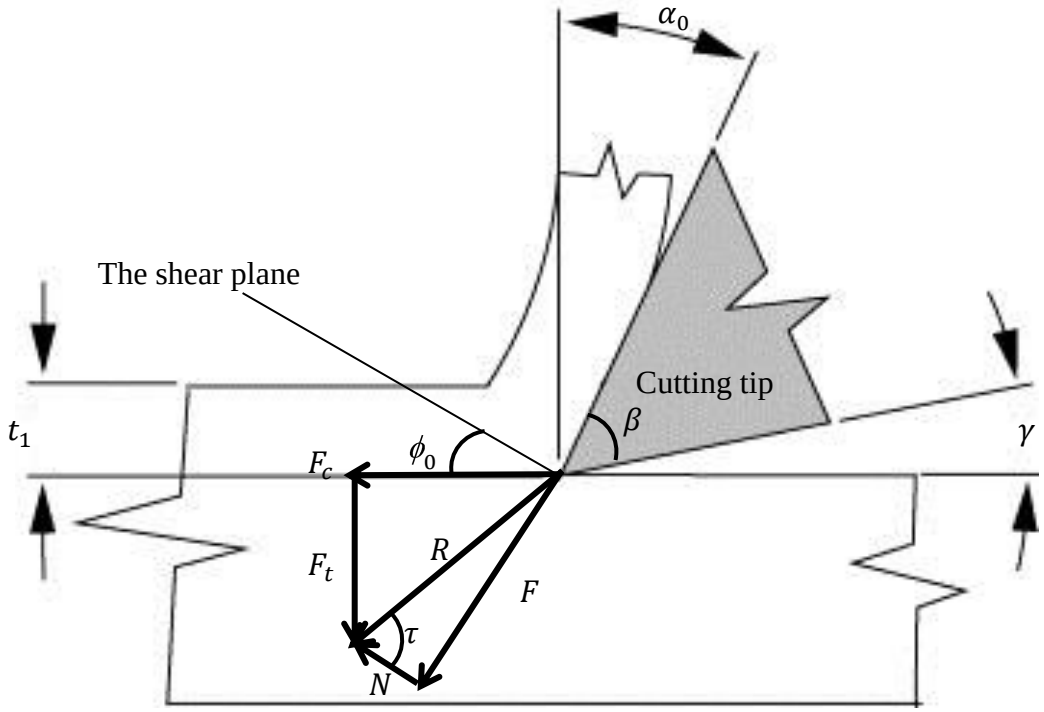

Fig. 3.8. Illustration of the force components and angles in orthogonal cutting: F_c is the cutting force along the tool travel direction; F_t is the thrust force normal to the travel direction; F is the friction force that resists the movement of the chip while N is the normal force; R is the resultant force.

$$F_c = \frac{\cos(\tau - \alpha_0)}{\cos(\phi_0 + \tau - \alpha_o)} \frac{\tau_s b t_1}{\sin(\phi_0)}, \tag{3.32}$$

where F_c is the cutting force, whose direction is along to the tool travel direction, α_0 is the tool rake angle, ϕ_0 is the shear angle, which is between the shear plane and the work surface, τ is the friction angle, which is related to the friction coefficient μ and

$\mu = \tan^{-1}\tau$, t_1 is the underformed chip thickness or depth of cut, b is the uncut chip width in three dimensional cutting, τ_S is the material shear strength under cutting conditions.

The shear plane angle can be predicted by Ernst-Merchant model or Lee-Shaffer model. The first model is based on the minimizing force and Lee-Shaffer model is based on slip line theory.

The criterion used by Ernst and Merchant, 1941, was to select ϕ_0 so as to minimize the magnitude of the resultant force. The predicted shear angle is (Ernst and Merchant, 1941),

$$\phi_0 = 45° - \frac{\tau - \alpha_0}{2}. \tag{3.33}$$

The shear plane angle is predicted by Lee-Shaffer (Lee and Shaffer, 1951) is,

$$\phi_0 = 45° - (\tau - \alpha_0). \tag{3.34}$$

The friction angle $\mu = \tan^{-1}\tau$ where μ is the friction coefficient, thus for the same cutting condition, the friction coefficient keep same. For the positive rake angle, there is a relationship between positive rake angle, tool angel, and the flank angle.

$$\beta = 90° - \alpha_o - \gamma, \tag{3.35}$$

where β is the tool angle, γ is the flank angle. Thus as the rake angle increases, the shear angle increases, then the cutting force decreases.

3.6 Two-dimensional photo-elastic fringe patterns of rigid cones

From the previous discussion, the location of first yield due to the contact between a cone and a flat surface is on the surface and nearby the apex of the cone. To observe the live stress distribution and failure caused by a conical contact, a photoelasticity system is set up. The two-dimensional photo-elastic fringe patterns of rigid cones are captured as a function of increment in the contact load. The rigid cone tool model with the semi-angle 30° is made from stainless steel. A normal load is applied and the rigid cone tool contacts the elastic plate which is made from Lexan polycarbonate sheet. Figure 3.10 shows the development of the stress fringe patterns as a function of increment in the contact load. The cone penetrates the plate with a velocity 0.02 mm/ time. The location of the facture of the elastic plate is on the rigid surface.

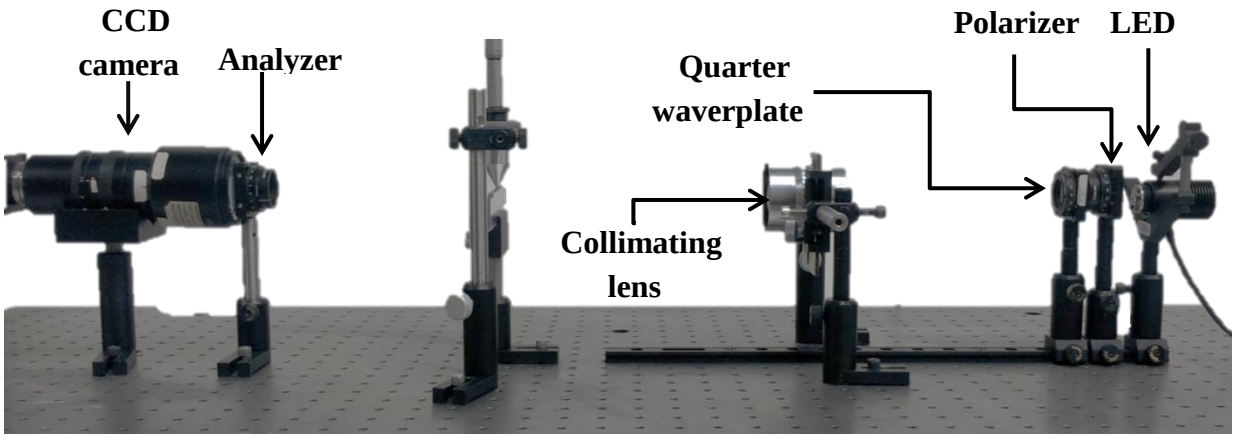

Fig. 3.9. Photoelasticity system developed at CHLST labs.

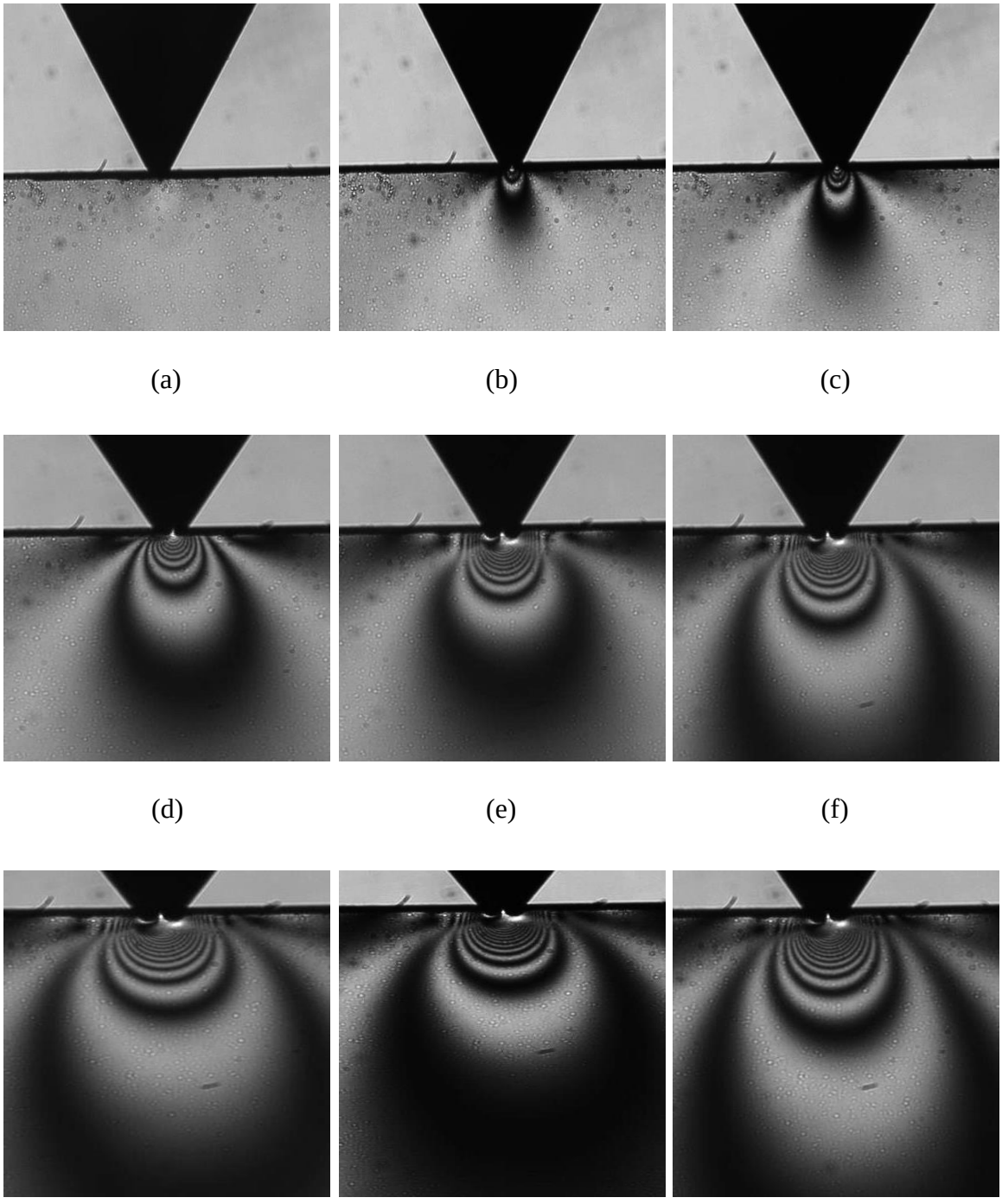

(a) (b) (c)

(d) (e) (f)

(g) (h) (i)

Fig. 3.10. Photoelastic stress fringe patterns of rigid cone: a pure normal load is applied by a rigid cone with semi-angle of 30°. As the load is increased, the number of fringes representing the stress distribution within the plate increases, as shown from (a) to (i).

4. Finite element analysis

4.1 Introduction

Cutting process is a very complicated; it is influenced by the material mechanical properties, failure property, cutting tool geometry, cutting speed, depth of cut and width of cut, as well as the friction between cutting tool and the specimen. During the cutting process, the friction between cutting tool and specimen also causes the thermal conductivity. Researchers are trying to find the best cutting conditions and tool geometries to optimize process efficiency. Although the results could be obtained by experimental works, they are time-consuming and expensive. In addition, simple analytical methods have limited application to explain the cutting process. Thus, numerical methods are becoming more important.

4.1.1 Introduction of Abaqus

In recent years, commercial finite softwares such as Abaqus, ANSYS, COMSOL, etc. have been used popularly in academic and industrial areas for computer-aided design and analysis. Because the cutting analysis is a complicated dynamic analysis involving contact, plasticity, large deformation and element failure, the commercial finite software, which has a significant application for nonlinear dynamic and high deformation problems, is required. Abaqus was first released in 1978 including three main analysis products: Abaqus/Standard, Abaqus/Explicit, and Abaqus/CFD. Abaqus/Standard is popularly

used for static equilibrium problem in structural simulations while Abaqus/Explicit is better in applications for the nonlinear dynamic and high deformation problems. Abaqus/CFD is a computational fluid dynamic analysis package. Based on the requirements of the cutting process analysis, Abaqus/Explicit is used for the analysis.

In this Section, the procedure of finite element analysis in Abaqus and some critical problems are presented. The finite element results are compared with the analytical results for verifications.

4.2 Chip separation criterion

4.2.1 Finite element approach

In finite element methods, the displacement-based finite element analysis is used popularly since it reduces computational time. In this Section, the basic equations for standard displacement-based finite element analysis are described (Abaqus, 2013).

Let $\{f\}$ be the vector of displacement at any point of the element, and the vector of nodal displacements of an element could give the vector of displacement at any point of the element by interpolation functions

$$\{f\} = [N]\{\delta\}^e, \tag{4.1}$$

$\{N\}$ is the matrix of shape functions serving as interpolation function, and $\{\delta\}^e$ is the vector of nodal displacements at any point of the element.

From the linear elastic mechanics, the element strain is associated with the nodal

displacement of an element

$$\{\varepsilon\} = [B]\{\delta\}^e , \tag{4.2}$$

$\{\varepsilon\}$ is the vector of strain at any point of the element and $[B]$ is the strain-displacement matrix that transforms nodal displacement to strains at any point in the element.

The stresses in individual elements is given as

$$\{\sigma\} = [D][B]\{\delta\}^e , \tag{4.3}$$

$\{\sigma\}$ is the vector of stress at any point of the element and $[D]$ is the elastic matrix related to the material elastic properties.

According to the virtual work principle, the work-equivalent nodal force could be given

$$\{F\}^e = [k]^e \{\delta\}^e , \tag{4.4}$$

where $\{F\}^e$ is the work-equivalent nodal force vector and $[k]^e$ is the element stiffness matrix.

Using the direct stiffness method, combine the elements and get the entire structure stiffness matrix and all elements equivalent nodal force vector. Since the nodal displacement at the common nodes in the neighbor elements is same, the structure stiffness matrix $[k]$, the force vector $[F]$ and the nodal displacement vector of all elements $[\delta]$could be related as

$$\{F\} = [k]\{\delta\} . \tag{4.5}$$

Thus, in the finite element analysis, the nodal displacement in the structure could be used to get nodal displacement at any point in the element, then get the stress at any point in the element.

4.2.2 Element failure model

The process of cutting is the process of material dynamic failure process. Abaqus supplies two element failure models: shear failure model and tensile failure model. The shear failure model uses the equivalent plastic strain as a failure measure. The tensile failure model uses the hydrostatic pressure stress as a failure measure to model dynamic spall or pressure cutoff. In this Section, the shear failure model is used to analyse the cutting process.

The shear failure model is based on the value of the equivalent plastic strain at element integration points; failure is assumed to occur when the damage parameter exceeds 1. The damage parameter, ω, is defined as

$$\omega = \frac{\bar{\varepsilon}^{pl} + \sum \Delta\bar{\varepsilon}^{pl}}{\bar{\varepsilon}_f^{pl}}, \tag{4.6}$$

where $\bar{\varepsilon}^{pl}$ is any initial value of the equivalent plastic strain. $\Delta\bar{\varepsilon}^{pl}$ is an increment of the equivalent plastic strain and $\bar{\varepsilon}_f^{pl}$ is the strain at failure (Abaqus, 2013).

4.2.3 Element removal

When the shear failure criterion meets at an integration point, all the stress components will be set to zero and that material point fails. By default, if all of the material points at any one section of an element fail, the element is removed from the mesh. The cutting model using the splitting line is defined for the cutting process analysis. This model contains 4 parts: cutting tool, uncut chip, splitting line, and base, which are shown in Fig. 4.1. The uncut chip, splitting line, and base are considered as a single part and defined the specimen. Define the fracture stress/strain as the shear failure criterion to the splitting line, thus when the plastic deformation of the element of the splitting line meets the shear criterion, the element is removed leading to the chip separating from the base. For an accurate failure model, the material elastic and plastic properties are necessary.

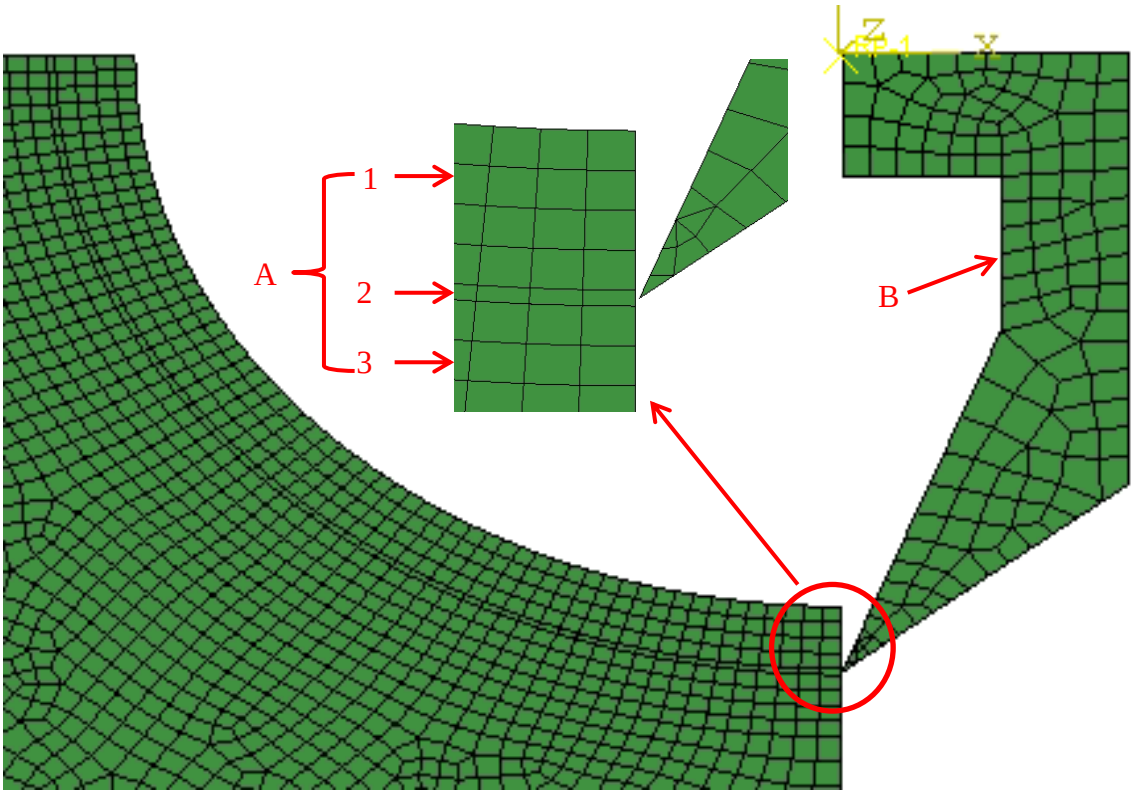

Fig. 4.1. Element failure model uses the splitting line for cutting process analysis in Abaqus. (A) is the specimen, and (B) is the cutting tool. In the specimen, (1) is the uncut chip; (2) is the splitting line; (3) is the base. In Abaqus, the element failure criterion is defined on the splitting line, thus the element of the splitting line is removed when the deformation or stress of elements in the splitting line meets the failure criterion in order to separate the uncut chip from the specimen.

4.3 Model definition

In the cutting model using splitting line, there are 4 parts including uncut chip, splitting line, base, and cutting tool.

The cutting tool geometry is shown in Fig. 4.2(a). The height of the cutting tool is 1.0mm. The rake angle is $\alpha_0 = 20°$, the tool angle is $\beta = 30°$, and the flank angle is $\gamma = 40°$.

The uncut chip thickness is uniform, which is 0.1 mm, and the angle is 90°, which is shown in Fig. 4.2(b). The splitting line thickness is also uniform, which is 0.01 mm, and the angle is 90° as shown in Fig. 4.2(c). The base height is 3.0 mm and length is 3.0 mm, and the angle is 90°.

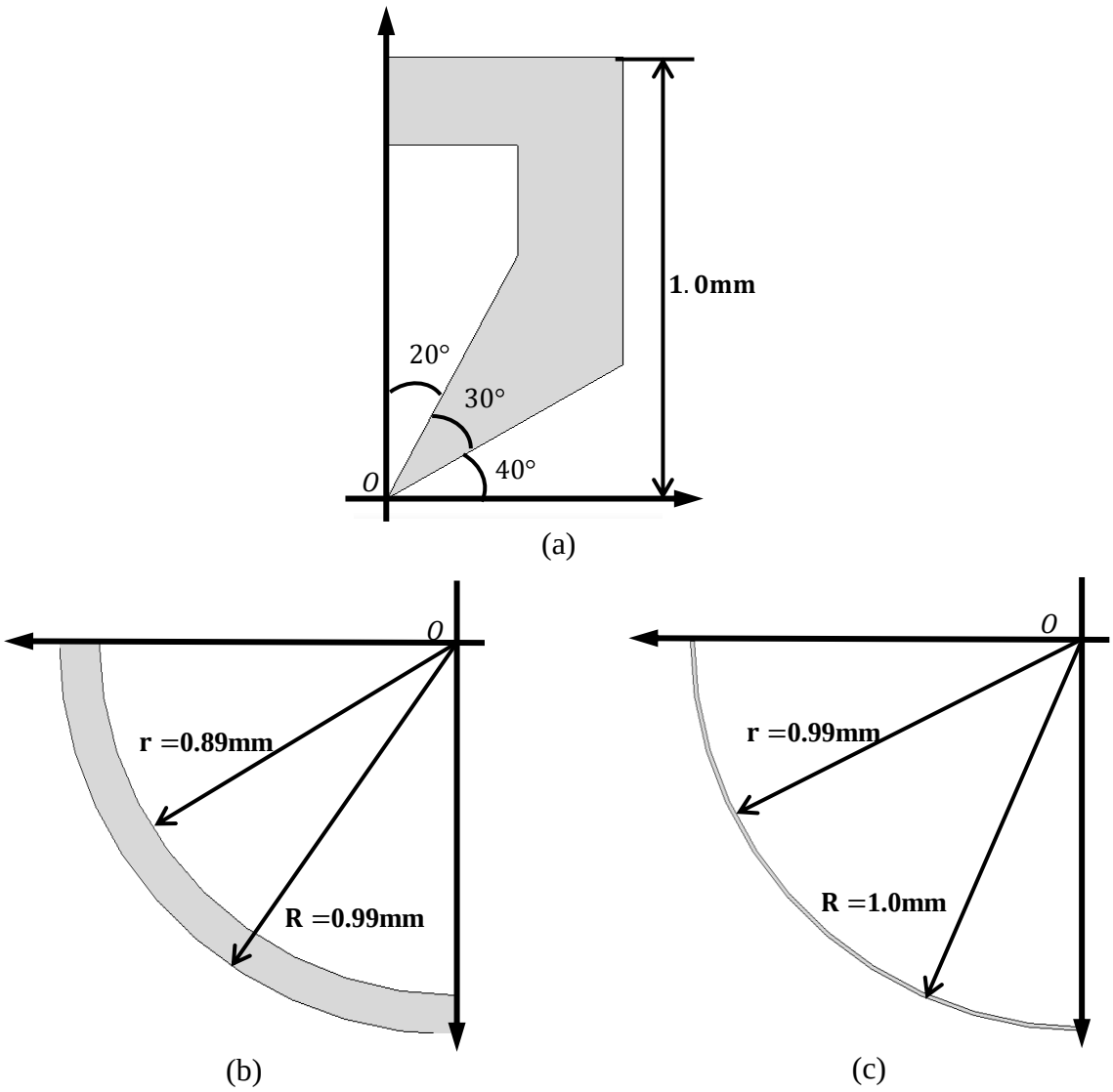

Fig. 4.2. Cutting tool geometry: (a) the cutting tool; (b) the uncut chip; (c) the splitting line.

4.4 Material properties definition

In Abaqus, to simulate the cutting process, the material model must have defined the mass density, elastic or hyperelastic properties, plastic stress-strain, and the failure criterion. In this Section, the structure and hyperleastic properties of a representative biological sample are presented. However, because of the limited information about the plastic stress-strain and the failure criterion of biological samples a linear elastic and linear plastic material model is utilized in the cutting process simulations.

4.4.1 Biological samples structure and mechanical properties

As the medical development, the structure and mechanical properties of biological sample are required for the development of medical device and therapies. In recent years, more and more researches about the biological sample mechanical properties are being released.

A representative biological sample, for example, the soft representative biological sample is a group of tissue which binds, supports and protects body and structures and organs, for example, tendons, blood vessels and skin (National Cancer Institute, 2013). They are distinguished from hard tissue such as bones for their high flexibility and soft mechanical properties.

The fiber-reinforced composite structures are the main characteristic of the soft representative biological sample and their mechanical behavior is strongly influenced by

the concentration and structural arrangement of constitute such as collagen and elastin (Fung, 1993).

The soft representative biological sample behaves anisotropically, since the fibers have preferred directions. In a microscopic sense they are non-homogeneous materials because of their composition. The tensile response of the soft representative biological sample is nonlinear stiffening and tensile strength depends on the strain rate. In contrast to hard tissues, the soft biological sample may undergo large deformations. Even though some soft biological samples have hyperelastic properties, the stress-strain curve is a typical J-shaped (tensile), as shown in Fig. 4.3.

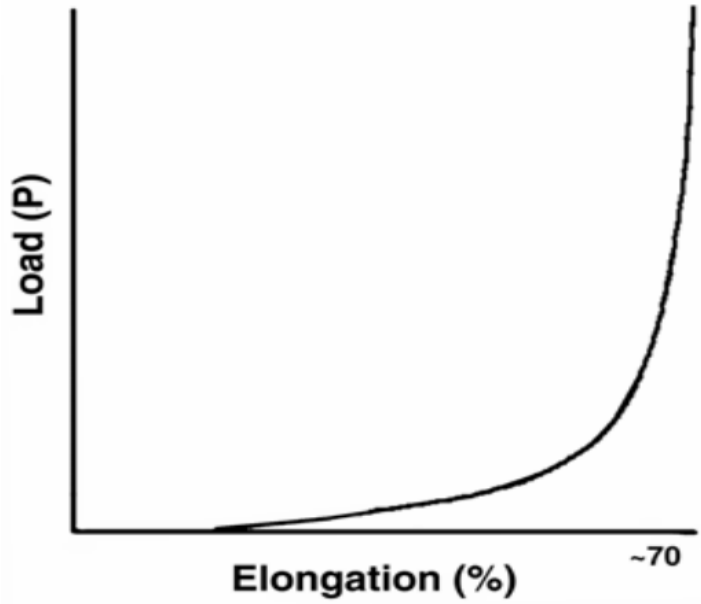

Fig. 4.3. Load-elongation curve for a ligamentum flavum tested in tension to failure (Nachemson and Evans, 1968).

4.4.2 Limitation of modeling biological sample fracture in Abaqus

In Abaqus, there are two methods to define a hyperelastic material model, which are tensile or shear experiment data and the stain energy potential defining the strain energy stored in the material per unit of reference volume as a function of the strain at that point in the material. The strain energy potentials models include Ogden and Mooney-Rivilin for hyperelastistic material. However, for the large deformation and element failure analysis, the plastic stress/strain, an element failure criterion, must be defined in Abaqus, there are few publications about the plastic deformation, stress and failure. Thus, the material model is not totally defined and the analysis cannot be conducted. For the cutting analysis, a linear elastic and linear plastic material model is defined in Section 4.4.3.

4.4.3 Material properties definition

In Abaqus, when the element deformation or stress meets the shear failure criterion, the element is removed in order to obtain the chip separated from the original model. Thus the original model, which is nominated as specimen in previous section, contains uncut chip, splitting line and the base. Define the failure criterion to the splitting line. Then, when the elements in the splitting line meet the criterion, the elements are removed and the chips fall off. The mass density of the specimen is assumed to be $8250 kg/m^3$, the Young's modulus $2.2\times10^8 Pa$, and the Poisson's ratio 0.3, as recommended in Fung,

1993. The plastic stress-strain is linear, Fig. 4.4.

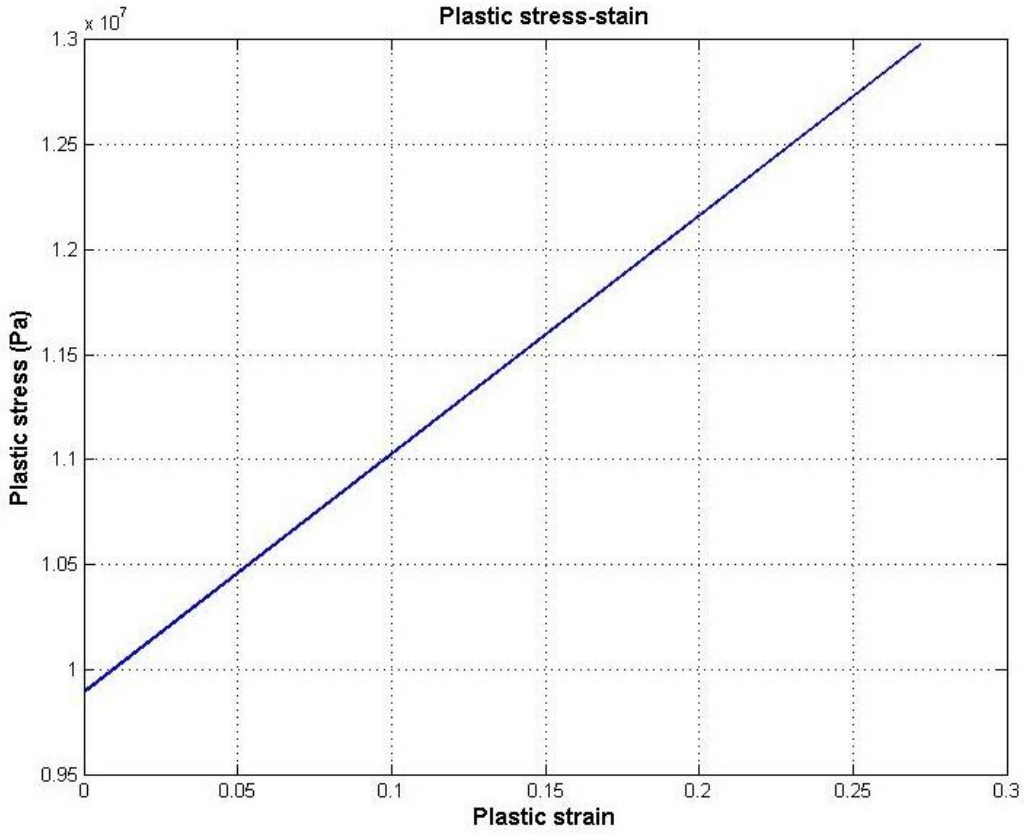

Fig. 4.4. Definition of material plastic stress-strain in Abaqus. Abaqus splits the material elastic and plastic stress strain curve into two separate parts including elastic stress-strain curve and plastic stress-strain curve. The plastic strain starts from 0.

The linear elastic and linear plastic material model is not appropriate and unrealistic definition for the biological material, which has high density and elasticity modulus. However, the cutting analysis is a complicated dynamic analysis involving contact, plasticity, large deformation and element failure, there will be significant mesh distortions causing the instability of the analysis during the analysis. Due to the influence of the

material properties including the mass density, elastic properties, and plastic property to the analysis stability, a material model with appropriate definition is required. Several material models are used, and the above material model gets a relatively stable result, which is not appropriate definition for a biological material but a required procedure.

For modeling purposes only and to insure rigidity, the cutting tool density is assumed to be $15000 kg/m^3$. In contrast to the specimen, the Young's modulus of the cutting tool is $8.0 \times 10^{12} Pa$ and the Poisson's ratio is 0.2. Thus, the cutting tool is rigid, and it does not undergo any deformations. The comparison of the materials' properties is shown in Table 4.1.

Table 4.1. Comparison of assumed specimen and cutting tool material properties*.

	Specimen Material Properties	**Cutting tool Material Properties**
Mass density (kg/m^3)	8250	15000
Young's modulus (Pa)	2.2×10^8	8.0×10^{12}
Poisson's ratio	0.3	0.2

* For modeling purposes only. For more specifics see Fung, 1993.

4.5 Definition of mesh

4.5.1 Definition of mesh element type

Finite element analysis is the method that the geometry under consideration is divided in large number of small elements. In two-dimensional analysis, the triangles or quadrilaterals are used typically as shown in Fig. 4.5.

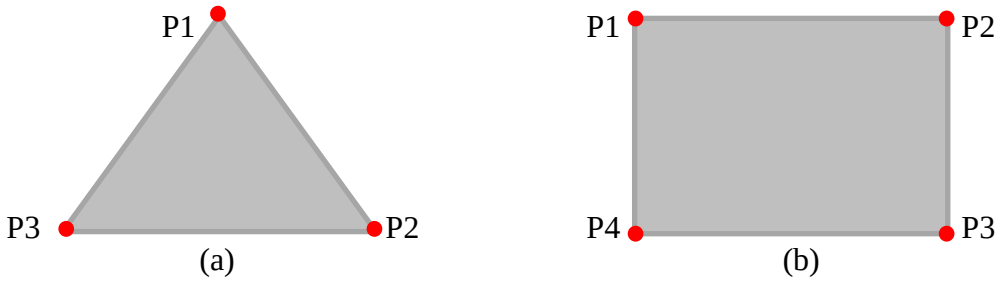

Fig. 4.5. Finite elements: (a) the triangle element; (b) the quadrilateral element.

In two-dimensional stress/displacement analysis, Abaqus supplies continuum elements for complex nonlinear analyses involving contact, plasticity, and large deformations. For the stress/displacement analysis, element CPS4R is selected, which is a 4-node bilinear plane stress quadrilateral, reduced integration, hourglass control element type (Abaqus, 2013). For a reduced-integration element, the displacement solution is more accurate and the analysis accuracy is not affected even when the mesh has a significant distortion (Abaqus, 2013). In contrast to the full-integration element, the reduced-integration has only one integration point; the stress on the integration point is

relatively accurate. The difference between full-integration element and reduced-integration element is shown in Fig. 4.6.

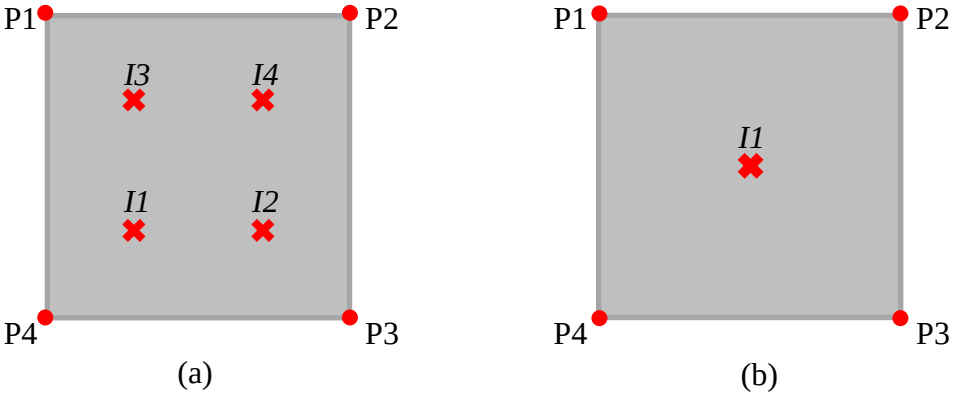

Fig. 4.6. Integration elements: (a) full-integration element; (b) reduced-integration element.

4.5.2 Definition of mesh element size

In order to find the influence of the element size to the accuracy of the analysis result, three meshing models are conducted. The numbers of elements of these three meshing models are shown in Table 4.2.

Table 4.2. Number of elements in three meshing models.

Model	**Number of elements**			**Total number of elements**
	Uncut chip	**Splitting line**	**Base**	
Model 1	**320**	**80**	**3330**	**3730**
Model 2	**400**	**100**	**4001**	**4501**
Model 3	**480**	**120**	**4554**	**5154**

The finite element results shown in Fig. 4.7 reveal that for different meshing models, the cutting force is almost same. In contrast, the stability of the result is affected by the meshing models. There are significant fluctuation on the results of model 1 and model 3, and the result plot of model 2 is relatively smooth. Thus, considering the accuracy and stability of the finite element analysis result, the meshing model 2 is selected, which defines the mesh size.

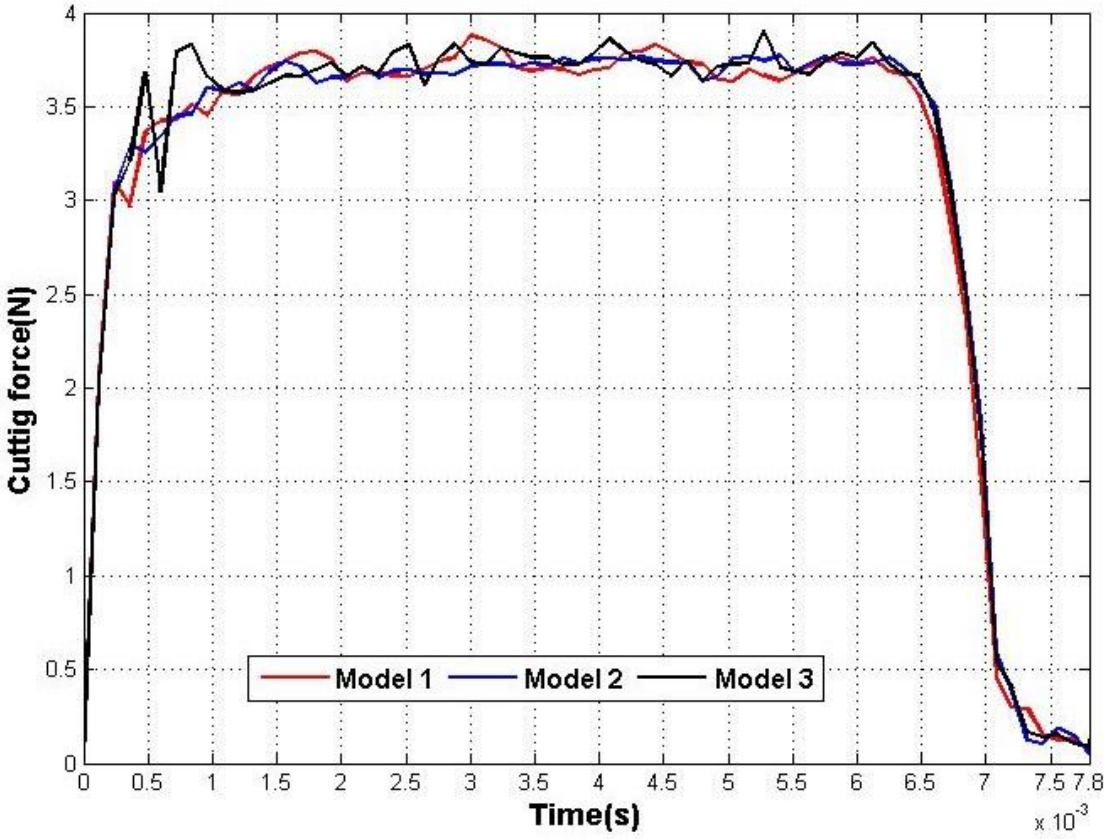

Fig. 4.7. Finite element results of three meshing sizes.

4.6 Definition of boundary condition

4.6.1 Surface contacts

4.6.1.1 Surface contacts in specimen

There are two pairs of surface contact between the parts in specimen, which are uncut chip bottom surface and the splitting line up surface, as well as, the splitting line bottom surface and the base up surface. These surface contact properties are same. The surface contact tangential friction is "Rough" leading to no slip will occur as long as the surfaces are in contact and in the normal contact "don't allow the separation after contact," (Abaqus, 2013).

4.6.1.2 Dynamic surface contacts between cutting tool and specimen

The contact between the cutting tool and the specimen is a dynamic contact. Assume the tool is rigid body and the specimen is deformable. The dynamic contact is the interaction between a deformable body and a rigid body.

A is a point on the deforming mesh of specimen with current coordinate X_A. *C* is a point in the cutting tool with the current coordinate X_C. A' is the closest point on the surface of the cutting tool to *A* at which the normal to the surface of the cutting tool, $\vec{n}$, pass through *A*. $\vec{r}$ is the vector from *C* to A'. The geometry described is shown in Fig. 4.8. Define the distance between *A* and A' is ***h*.** From the definitions introduced above

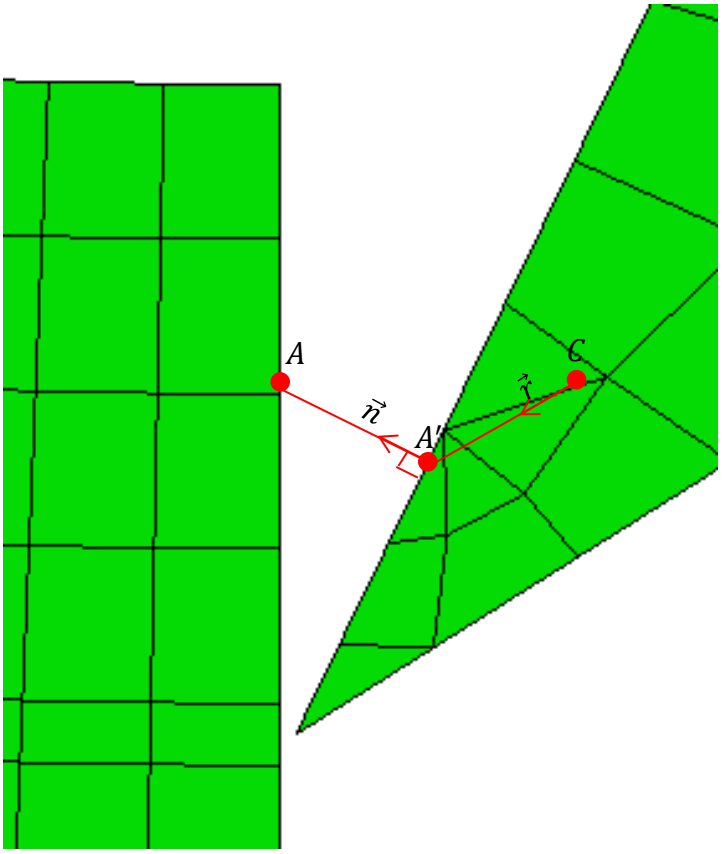

Fig. 4.8. Illustration of dynamic contact between tool and specimen.

$$\vec{n} \cdot h = -\overrightarrow{X_A} + \overrightarrow{X_C} + \vec{r}. \tag{4.7}$$

Define c is the clearance below which contact occurs. If $h < -c$, the surfaces are not in contact at A, no surface interaction calculations need be done at this point. For a "Hard" contact $c = 0$ in Abaqus. If $h \geq -c$, the surface are in contact.

When point A and the cutting tool are moving, point $A^{'}$ is moving on the surface of the cutting tool. The movement of point $A^{'}$ consists of two parts: movement due to motion of the cutting tool and motion relative to the body. $\overrightarrow{S^{\alpha}}$ is the measure distance

along the tangents t_α to the surface at $A^{'}$.

$$\delta\overrightarrow{X_A} = \delta\overrightarrow{X_C} + \delta\overrightarrow{r}\big|_{\gamma\alpha} + \delta\overrightarrow{r}\big|_{\phi C} = \delta\overrightarrow{X_C} + \delta\overrightarrow{\phi_C}\times\vec{r} + \overrightarrow{t_\alpha}\cdot\delta\gamma_\alpha, \tag{4.8}$$

where $\delta\gamma_\alpha$ is the 'slip' of point $A^{'}$, and the normal $\vec{n}$ will also change due to rotation of the cutting tool surface and due to slip along the surface.

$$\delta\vec{n} = \delta\overrightarrow{n}\big|_{\gamma\alpha} + \delta\overrightarrow{n}\big|_{\phi C} = \delta\overrightarrow{\phi_n}\times\vec{n} + \frac{\partial\vec{n}}{\partial\overrightarrow{S_\alpha}}\cdot\delta\gamma_\alpha. \tag{4.9}$$

Substitution of Eq. 4.8 and Eq. 4.9 to Eq. 4.7, the linearization form of the contact equation becomes

$$\vec{n}\cdot\delta h + h\left(\delta\overrightarrow{\phi_C}\times\vec{n} + \frac{\partial\vec{n}}{\partial\overrightarrow{S_\alpha}}\cdot\delta\gamma_\alpha\right) = \delta\overrightarrow{X_A} + \delta\overrightarrow{X_C} + \delta\overrightarrow{\phi_C}\times\vec{r} + \overrightarrow{t_\alpha}\cdot\delta\gamma_\alpha. \tag{4.10}$$

For "Hard" contact $h = 0$, the linearized kinematic Eq. 4.10 becomes

$$\vec{n}\cdot\delta h = -\delta\overrightarrow{X_A} + \delta\overrightarrow{X_C} + \delta\overrightarrow{\phi_C}\times\vec{r} + \overrightarrow{t_\alpha}\cdot\delta\gamma_\alpha. \tag{4.11}$$

This equation could be split into normal and tangential components,

$$\delta h = -\vec{n}\cdot\left(\delta\overrightarrow{X_A} - \delta\overrightarrow{X_C}\right) + \left(\vec{r}\times\vec{n}\right)\cdot\overrightarrow{\phi_C}, \tag{4.12a}$$

$$\delta\gamma_\alpha = -\overrightarrow{t_\alpha}\cdot\left(\delta\overrightarrow{X_A} - \delta\overrightarrow{X_C}\right) - \left(\vec{r}\times\overrightarrow{t_\alpha}\right)\cdot\delta\overrightarrow{\phi_C}. \tag{4.12b}$$

For dynamic cutting analysis, the velocity and acceleration terms $\dot{h}$ and $\ddot{h}$ are used to calculate impact forces and impulse correctly.

$$\dot{h} = -\vec{n}\cdot\left(\dot{\overrightarrow{X_A}} - \dot{\overrightarrow{X_C}} - \dot{\overrightarrow{\phi_C}}\times\vec{r}\right), \tag{4.13a}$$

$$\ddot{h} = -\vec{n}\cdot\left(\overrightarrow{\ddot{X}_A} - \overrightarrow{\ddot{X}_C} - \overrightarrow{\ddot{\phi}_C}\times\vec{r}\right) + \vec{n}\cdot\overrightarrow{\dot{\phi}_C}\vec{r}\cdot\overrightarrow{\dot{\phi}_C} - \vec{n}\cdot\vec{r}\overrightarrow{\dot{\phi}_C}\cdot\overrightarrow{\dot{\phi}_C} - \left(\overrightarrow{\dot{X}_A} - \overrightarrow{\dot{X}_C} - \overrightarrow{\dot{\phi}_C}\times\vec{r}\right)\cdot\dot{\phi}_C\times\vec{n} + \frac{\partial\vec{n}}{\partial\overrightarrow{S_\alpha}}\overrightarrow{t_\alpha}\cdot\left(\overrightarrow{\dot{X}_A} - \overrightarrow{\dot{X}_C} - \overrightarrow{\dot{\phi}_C}\times\vec{r}\right) \quad (4.13b)$$

4.6.2 Node constrain of the specimen

The definition of boundary condition of the specimen is shown in Fig. 4.9. All the degrees of freedom of the nodes at the edges, which don't contact with the cutting tool, are constrained. Thus, during the cutting process the dynamic contact between the cutting tool and the specimen will not make the specimen moving.

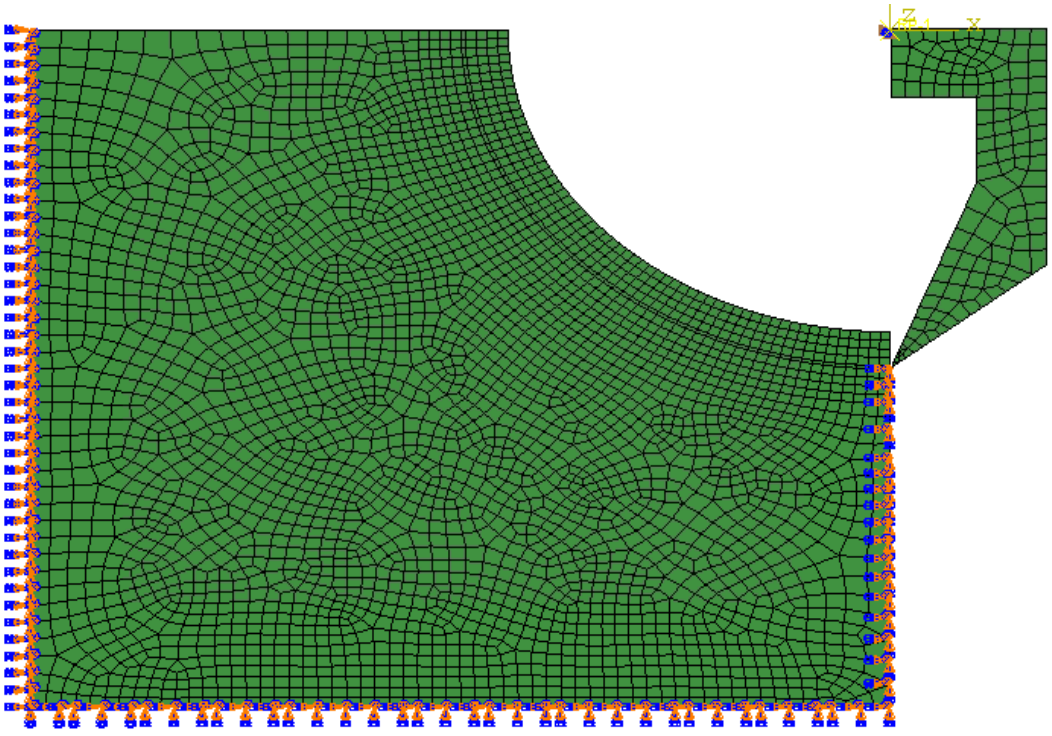

Fig. 4.9. Definition of boundary condition of the specimen in Abaqus: the constraint of all degree of freedom of the nodes at the specimen's edges makes sure the specimen not to move during the cutting process.

4.7 Definition of load condition

Reference Point (RP) is used to apply the load (Abaqus, 2013), which is shown in Fig. 4.10. Apply rotation speed to the reference point in order to lead the cutting tool to rotate taking the reference point as the rotation center. No translation in both x-direction and y-direction. The distance from the Reference Point to the tip of the cutting tool is 1.0 mm. The rotation/displacement is 2 radians/0.01s, which is around 1900 rpm. The load period or step is 0.012 s.

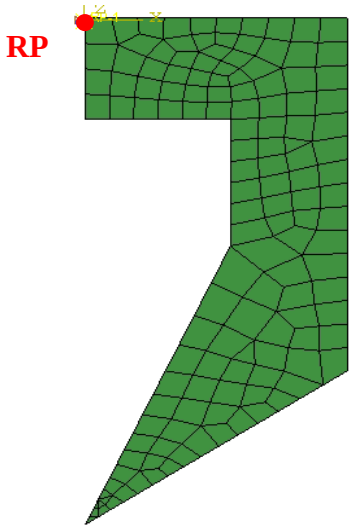

Fig. 4.10. Definition of load condition in Abaqus. Reference point is used to apply the load in Abaqus. In the rotational cutting process, the rotation speed is applied to the RP, and the tool rotates taking the RP as the rotation center at the applied rotation speed.

4.8 Stability analysis

The explicit procedure integrated through time by using many small time increments. Stable time increment is the one that leads to the convergence of analysis. In explicit dynamic analysis, the stable limit for the analysis is given in terms of the highest frequency $\omega_{\max}$ of the system as (Abaqus, 2013):

$$\Delta t \le \frac{2}{\omega_{\max}}. \tag{4.14}$$

However, the actual highest frequency in the system is based on a complex set of interacting factors, and it is not computationally feasible to calculate its exact value. In Abaqus/Explicit, an alternative method is used to estimate the stable time increment. The stable time increment is grossly estimated using the element length L^e and the wave speed of the material c^d

$$\Delta t \le \frac{L^e}{c^d}, \tag{4.15}$$

where $c^d = \sqrt{\frac{E}{\rho}}$. E is Young's modulus and ρ is the mass density. Thus as the number of elements increases for a specific model, the stable time limit decreases, which is shown in Table 4.3.

Table 4.3. Stable time increment of the models with different element sizes in Abaqus.

Model	Number of elements			Total number of elements	Max $\Delta t_{stable}(s)$
	Uncut chip	Splitting line	Base		
Model 1	240	60	2740	3040	5.02e-08
Model 2	320	80	3330	3730	4.56e-08
Model 3	400	100	4001	4501	4.13e-08
Model 4	480	120	4554	5154	3.34e-08

4.9 Results and discussions

The cutting tool with rake angle $\alpha_0 = 20°$, tool angle $\beta = 30°$, and flank angle $\gamma = 40°$. The height of the cutting tool is 1.0 mm. The distance between the cutting tip and the Reference Point is 1.0 mm. Apply the boundary condition of the rotation displacement/load to the Reference Point. The rotation boundary condition is 2 radians/0.01s, thus the rotation speed is around 1900 rpm, and the time period or step is 0.012s. The uncut chip thickness is 0.1 mm and length around 6.28 mm. The mesh element is CPS4R, which is a 4-node bilinear plane stress quadrilateral, reduced integration, hourglass control element type. There are 135 elements in cutting tool. Splitting line contains 100 elements, and 400 elements are in the uncut chip. In addition, there are 4001 elements in base. Define the shear failure criterion to the splitting line in order the chip separating the specimen when the cutting force is applied. The specimen

is deformable and the cutting tool is rigid. The magnitude of cutting force along time is shown in Fig. 4.11.

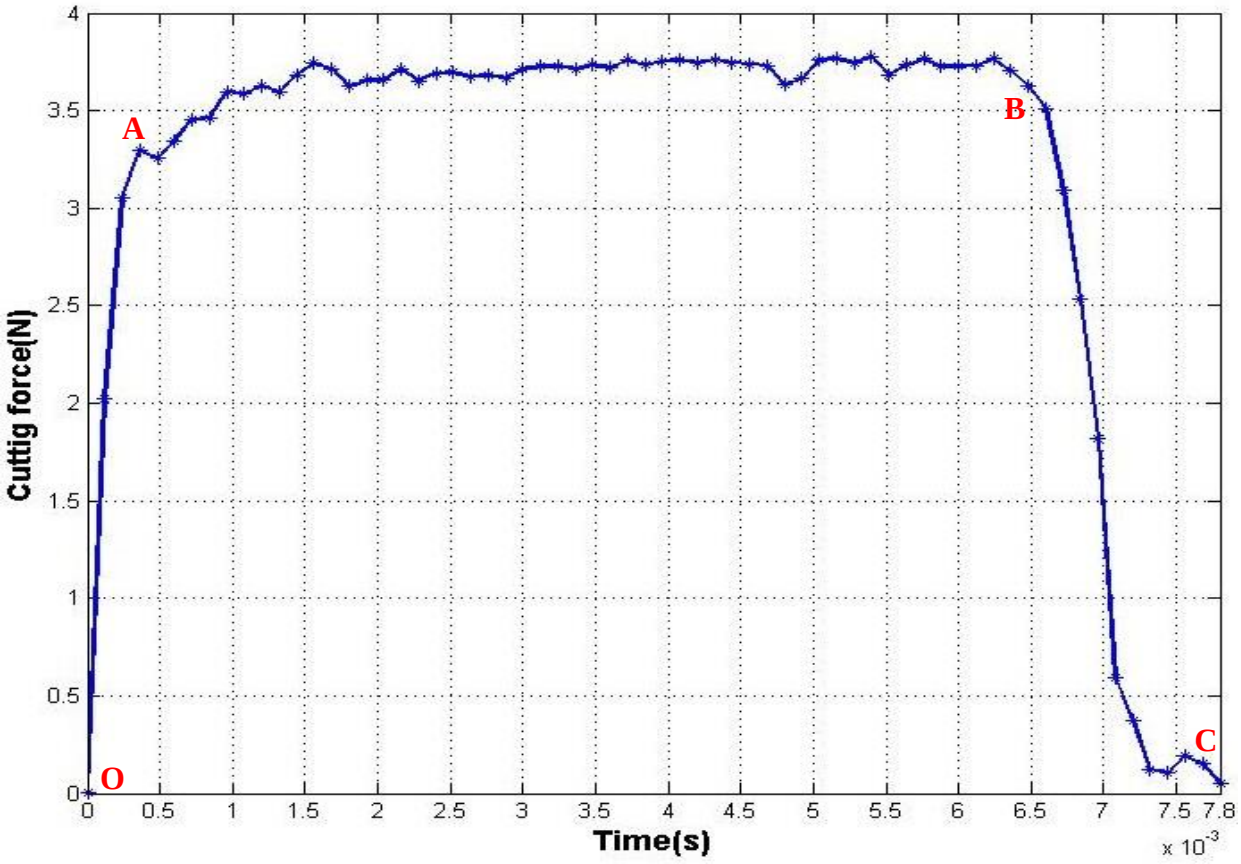

Fig. 4.11. Finite element result of the magnitude of the cutting force when the cutting tool rotation speed is 1900 rpm, and the uncut chip thickness is 0.1 mm. Point *O* represents the cutting tool contacts the specimen. From point *O* to point *A*, as the increment of the contact between the cutting tool and the specimen, the magnitude of stress on the contact surface is increasing due to elastic deformation. Point *A* represents the contact force is up to the ultimate stress. From point *A* to point *B* the force is up to material ultimate stress, the material is removed continuously till all the material is removed. From point *B* to point *C*, since the material is removed, and there is little or no contact between the cutting toll and the specimen, the magnitude of the cutting force decreases.

4.9.1 Fluctuations in the curve

The magnitude of cutting force is the stress or force on the integration point of each element in the splitting line when the integration point of the element meets the failure criterion, and the element is removed. In this analysis, the reduced-integration element is used and there is only one integration point in each element. Since the element failure is instantaneous and the failure happens element by element, thus the stress on the integration point of the element is output one by one, which is not constant leading to some fluctuations in the curve (Zhang et al, 2008).

4.9.2 Cutting process regions

The total cutting time is 0.0078 s, and there are three regions in the cutting process according to the material elastic/plastic deformation and fracture as shown in Fig. 4.11.

Region 1 is from point *O* to around point *A*. As the contact between the cutting tool and the specimen increases, the magnitude of stress on the contact surface is increasing and the deformation is elastic and plastic. Since the material mechanical property is linear elastic and linear plastic, the magnitude of contact stress is increasing linearly.

Region 2 starts from around point *A* to point *B*, where the elements are removed. As the cutting tool is keeping contacting the specimen, the magnitude of contact stress is increasing and the deformation is increasing too. When the contact stress or strain is up to the ultimate stress or ultimate strain, the material starts fracture or failure, thus the

elements in the splitting line are removed and the chip is separated from the base. The stress on the integration point of each element is the required stress or force to removing the material from the specimen.

Region 3 is from point *B* to point *C*, where the chip is separated from the specimen and the there is little or no contact between the cutting tool and the specimen. Thus the cutting force is decreasing. The material response and the cutting action are shown in Fig. 4.12.

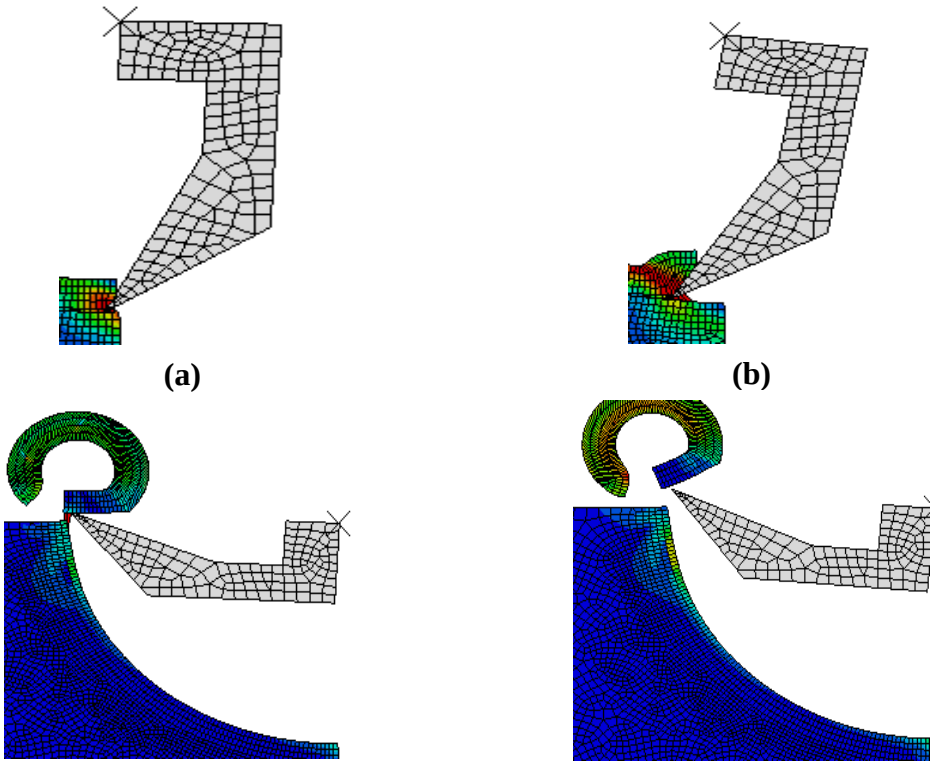

Fig. 4.12. Material deformation and fracture during the cutting process: (a) the cutting tool contacts the specimen, and there is elastic and plastic deformation in the specimen; (b) as the increment of contacts between the cutting tool and the material, the specimen starts to fracture; (c) the chip is almost separated from the specimen; (d) the chip is totally separated from the specimen.

4.10 Rake angle analysis

The cutting tool rake angle is changing from 10°, 20° to 30°, where the flank angle keeps 40°. Thus the cutting tool angle is decreasing from 40°, 30° to 20°. The simulations are running respectively at rotation speed around 1900 rpm. According to the previous theoretical study, as the tool angle decreases, the force causing the elastic-plastic deformation and facture decreases. The finite element analysis results plot in Fig. 4.13.

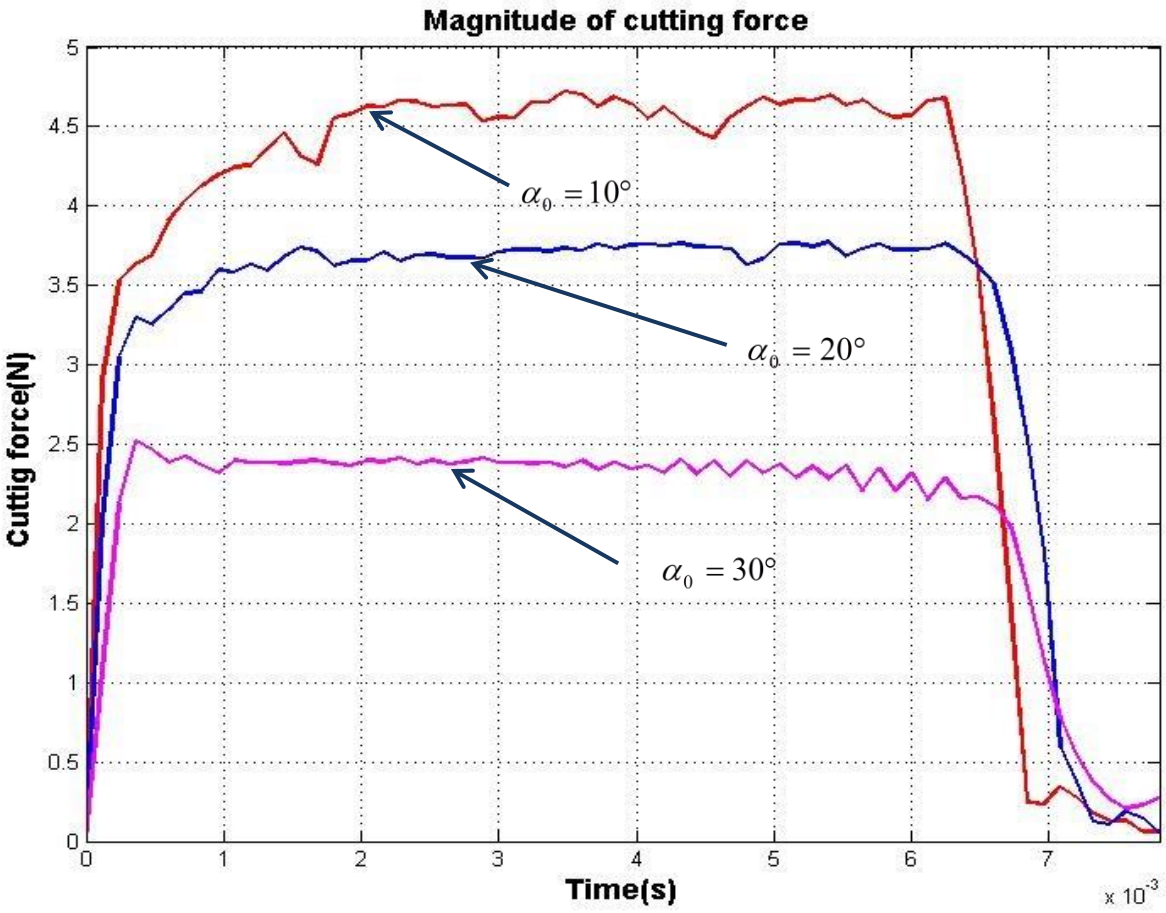

Fig. 4.13. Comparison of magnitude of cutting force of the cutting tools with rake angle 10°, 20°, and 30° when the cutting rotation speed is 1900 rpm, and the uncut chip thickness is 0.1 mm.

Table 4.4 shows the comparison of finite element analysis results and analytical result from Eq. 3.32. In Eq. 3.32, τ_s is the material's shear stress under cutting condition. In Abaqus, the material's failure model is defined by the shear stress/strain, thus when the material shear stress/strain is up to the shear stress/strain, the material is removed. Thus τ_s is equal to the model shear failure stress.

In addition, the entire model is in millimeter scale, for 2-dimensional simulation, the width of cutting is 1.0 mm. The depth of cutting is 0.1 mm, which is defined in Chapter 3. Thus, the analytical and FEM cutting force results are shown in Table 4.4.

Table 4.4. Comparison of analytical and FEM results of the magnitude of the cutting force.

Rake angle	**10°**	**20°**	**30°**
Average cutting force by FEM (N)	**4.47**	**3.68**	**2.39**
Ratio of FEM results to the FEM result of the model rake angle 10°	**1**	**0.8233**	**0.5347**
Cutting force by orthogonal cutting method in Chapter 3 (N)	**4.70**	**3.92**	**3.23**
Ratio of analytical results to the analytical result of the model rake angle 10° in Chapter 3	**1**	**0.8340**	**0.6872**
Error $(F_{analytical} - F_{FEM})/F_{FEM}$	**0.05**	**0.07**	**0.35**

Thus, when the rake angle is increasing and the tool angle is decreasing, the required load for achieving the yield criterion is decreasing, which is same as the conclusion using contact mechanics in Chapter 3.

5. Preliminary biological sample cutting experiments

The preliminary biological sample cutting experiments are conducted to find the characters of the biological sample cutting and the influence of the rake angle of the cutting tool on the cutting force.

5.1 Experiment system set up

The major components of the experiment are electrical motor, a torque coil, two torque transducers, and tested cutting tool. The scheme of the experiment set-up is shown in Fig. 5.1.

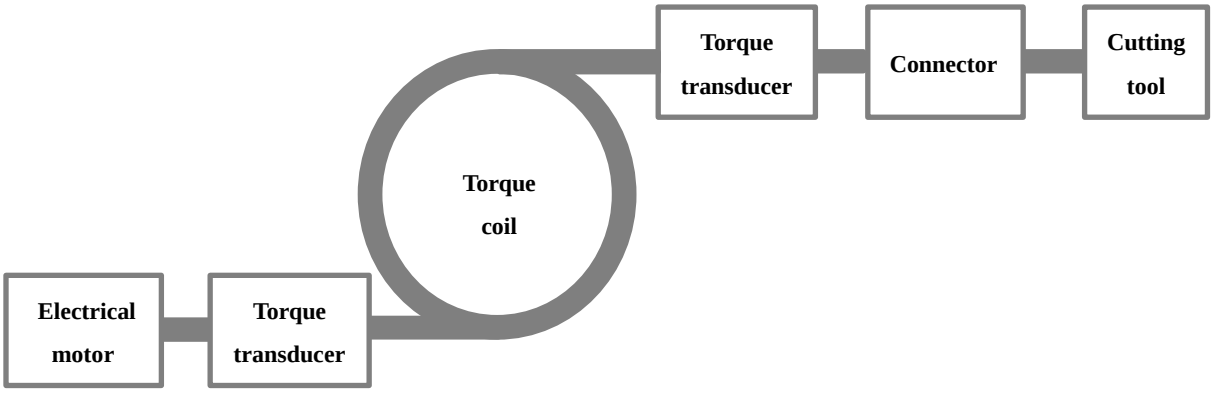

Fig. 5.1. Scheme of preliminary biological sample cutting experiment using torque coil as the power transmission for the rotational cutting actions.

The torque transducer between the electrical motor and the torque coil is used to record the motor torque and the torque transducer between the torque coil and the cutting tool is used to monitor the cutting torque.

5.2 Biological sample cutting experiment result

The cutting tool with a flat or straight cutting edge was test at rotation speed 1000 rpm. The outer diameter is 3.5 mm. During the cutting process, the data of torque was captured versus times. The cutting toque was recorded by the torque transducer between torque coil and the cutting tool. The plot of cutting torque versus time is shown in Fig. 5.2.

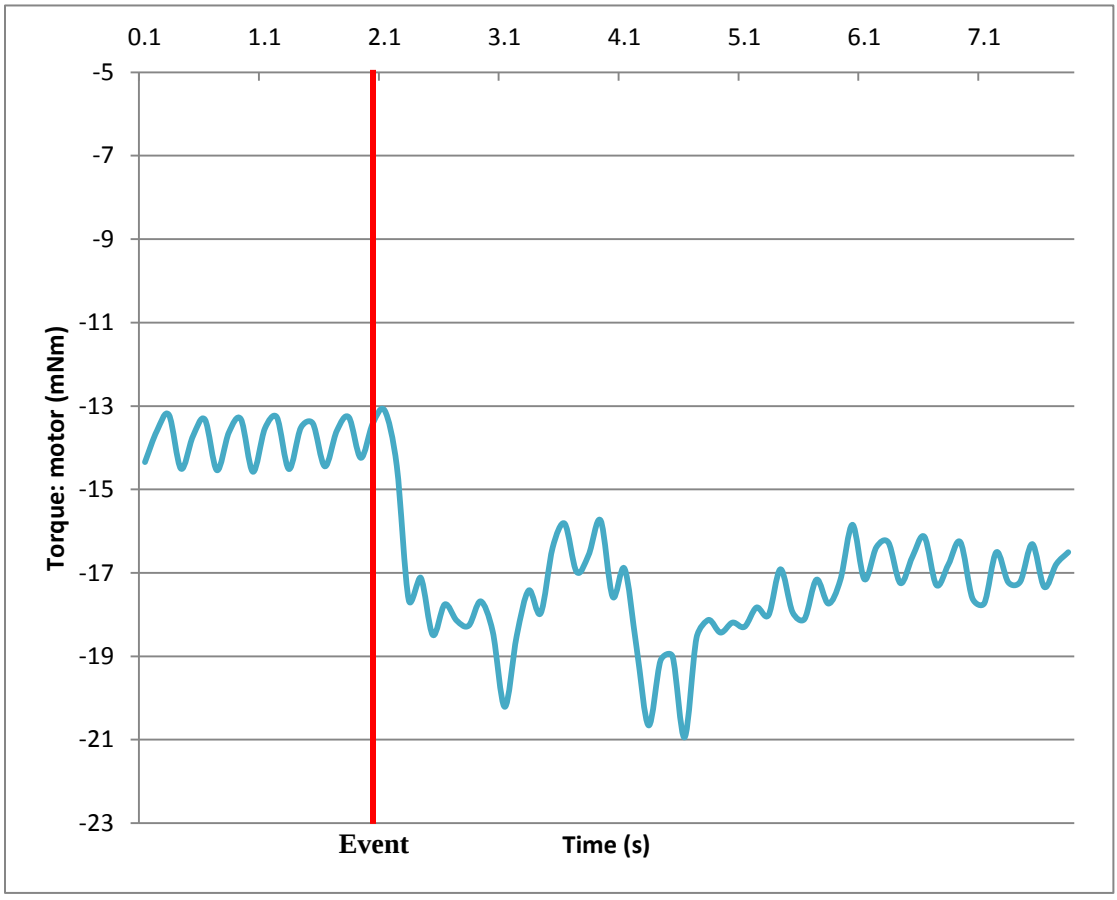

Fig. 5.2. Raw experimental data from preliminary biological sample cutting experiment at rotation speed 1000 rpm. "Event" represents the instant when the tool contacts the sample.

The experiment data reveals that the cutting path appeared to be formed by a repeated sequence of localized deformation followed by localized fracture. When the cutter contacts the sample, the magnitude of torque increased as the sample deformation reached a peak, then the magnitude of torque suddenly dropped as onset of localized fracture extension occurred, which corresponds with the finite element analysis results, as shown in Fig 4.11.

5.3 Biological sample cutting experiments of using different cutting tools

Two different cutting tools were used in the preliminary biological sample cutting experiments, which is shown in Fig. 5.3. Both tools' outer diameter is 2.6 mm. The length of cutting window is 4.0 mm and the width of cutting window is around 2.0 mm. The tools' geometries are listed in Table 5.1.

(a) (b)

Fig. 5.3. Cutting tools used in experiments: (a) Tool A with a flat cutting edge, (b) Tool B with a teeth cutting edge. The outer diameter of both tools is 2.6 mm. The length of the cutting edge is 4.0mm, and the width of cutting window is 2.0 mm.

The cross sections of cutting tips of two cutters are shown in Fig. 5.4. The rake angle of Tool A is around 90° and the rake angle of Tool B is around 55°. The experiments focus on the influence of the rake angles of cutting tool on the cutting torque or force. The torque data versus time is captured by the torque transducer between the torque coil and the cutting tool. The results are shown in Fig. 5.5.

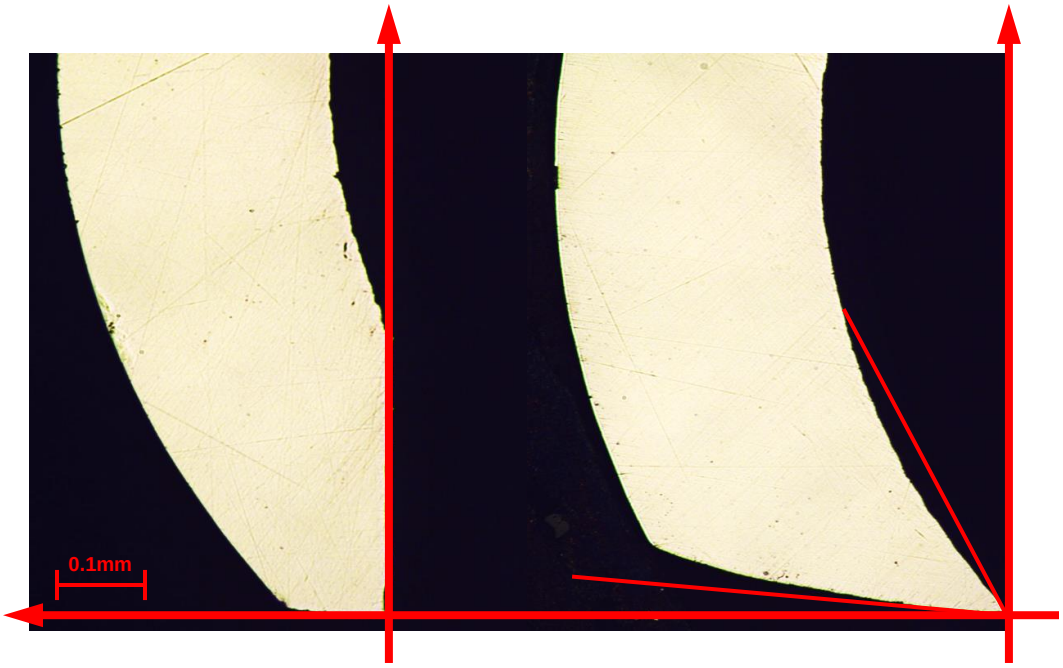

(a) (b)

Fig. 5.4. Cross section of the cutting edge of the tested tools: (a) Tool A; (b) Tool B. The cutting tool geometries are shown in Table 5.1.

Table 5.1. Cutting tools geometries of tested tools.

Cutting tool	O.D. (mm)	I.D. (mm)	Cutting window		Tool angle (degree)
			Height(mm)	Width(mm)	
Tool A	2.6	2.0	4.0	2.0	90
Tool B	2.6	2.0	4.0	2.0	55

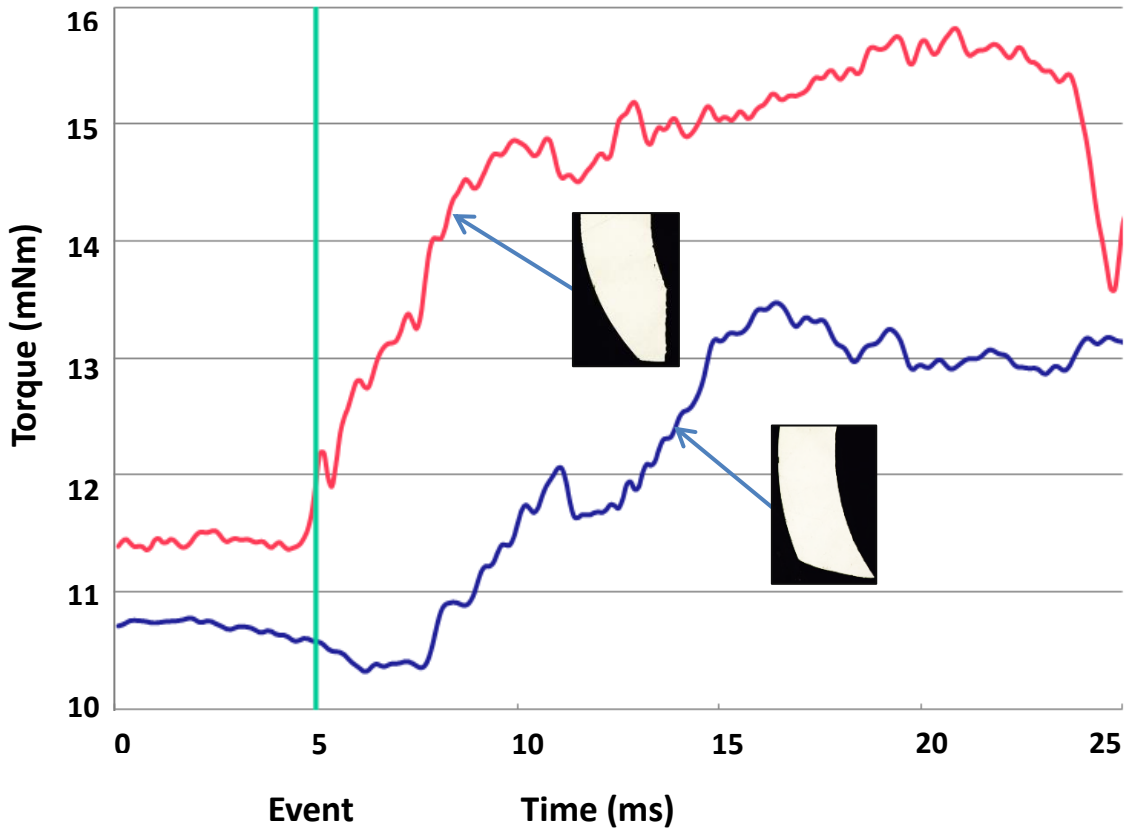

Fig. 5.5. Experimental results of the cutting torque for one revolution obtained by tested tools at rotation speed of 3000 rpm. "Event" represents the instant when the tool contacts the sample.

The magnitude of cutting torque of Tool B is smaller than the magnitude of cutting torque of Tool A, and the rake angle of Tool B is smaller than the rake angle of Tool A. The experimental result is same as the analytical and finite element analytical result.

6. Conclusions and discussions

Sample cutting is one of the important minimally invasive medical treatments. The sample cutting at the distal end of the devices is achieved by the power or cutting action transmission from the proximal tip to the distal end of the devices. Thus, for a biological sample cutting during a minimally invasive surgery, the transmission of the power or a cutting action from the proximal tip of the removal devices to the cutter at the distal end is crucial.

However, since the minimally invasive procedure is processed by inserting the devices into patient's body from a tiny aperture, the common characteristic of the sample cutting devices are long and slim. For example, the working length of the TurboHawk system is from 1100 mm to 1450mm, and the diameter is from 1.9 mm to 2.7mm. The length of the endoscopes working channel, which allows the endoscopic devices, for example, biopsy forceps, to pass through, is up to 2180 mm, and the diameter is from 0.75 mm to 6.0 mm.

The challenge of the sample cutting in the minimally invasive medical treatment is that enough power must be transmitted to the cutter at distal end of the devices for biological sample cutting, whose length is up to meters, and the diameter is in millimeters scale. Thus, an investigation of the potential powering mechanisms was conducted.

In addition, the power mechanism is used for powering a rotational cutting action. A cutter should be located at the distal end of the devices. Since the geometry of cutting

tool influences the required cutting power, the analytical and finite element analyses are used for the investigation of the cutting geometry. The contact mechanics and cutting mechanics are used for analytical analysis, and a commercial software, Abaqus, is used for finite element analysis. Analytical result shows that as the angle of the cutting tool decreases, the required magnitude of cutting force of material removal decreases.

However, the cutting process is relative complicated, there are limitations of the application of simple analytical analysis, thus the finite element analysis, Abaqus, is used.

For finding the characters of the biological sample cutting and the influence of the cutting geometries on the cutting force, the preliminary cutting experiments are introduced.

6.1 Powering mechanisms

Powering mechanisms were discussed including fluid, electrical, and torque coil. Though water/air is an inexpensive, clean and nontoxic power source for medical device, the energy lost during the flow in the pipe due to the friction between the fluid and the channel walls is increasing as the increment of transmission. Thus, fluid is not economical for a long-distance power transmission. In addition, there is a risk of damage to the body due to fluid pressure, if leaking were to occur.

The electrical method, where a DC motor is discussed, is a relatively accurate control. However, the maximum length of the motor is constrained by the rigid cutting tip of the

sample cutting device. When the length of DC motor is smaller than 15.0 mm, and the diameter is smaller than 4.0 mm, the output torque of current commercial productions is in micro Newton meter scale.

Torque coil, opposed to other methods, can accurately transmit the rotation between two objects if they are nonlinear and with some bent sections. In addition, for fluid and electrical mechanisms, there is a risk of damage to the body due to high fluid pressure or large electrical current is inside the body, whereas the application of a torque coil removes the risk. In aspects of design and manufacture, it is also much easier. The comparison of the potential mechanisms is shown in Table 6.1.

Table 6.1. Comparison of the potential power mechanisms.

	Compressed air/water	Electrical Micro motors	Torque coil
Power Transmission Efficiency	Decreases as the transmission length increases.	Directly connect to power supply.	Directly connect to a driver, for example, a motor.
Rotational motion generator	Turbines	Miniature DC motors	-
Rotational motion generator efficiency	The efficiency of gas turbines is up to 60%, and the efficiency of water turbines is up to 90%.	11%-12% for millimeter-scale motor. (Namiki, 2013).	The cutting device can be directly connected with the torque coil, thus the output efficiency is up to 1:1.
Applied to endoscopes	Suitable for endoscopes with short working channel.	Suitable for endoscopes with rigid insertion tube.	Suitable for endoscopes with flexible and long insertion tube.
Safety	Dangerous: it can damage the body due to fluid pressure, if leaking were to occur.	Good: the supplied voltage is 3V and the current is in mA. (Namiki, 2013). DC motors can be capsuled protecting the hazardous substance leaks from motors.	Excellent: no pressure or current in human's body. The torque coil is surrounded by a protection tube.
Manufacturability	It is relatively difficult to manufacture a millimeter-scale turbine using conventional machining methods.	The millimeter scale motors are available in the market, however the cost is relatively high.	The commercial production is available in various size.

6.2 Cutting tool geometry analytical

6.2.1 Cutting tool geometry analytical analysis

The goal of this thesis is the investigation of the power mechanisms for a rotational cutting action at the rigid distal end of endoscopes. Since the cutting geometry has influence on the cutting force or power, in this Section the theory of contact mechanics and orthogonal cutting mechanics are used to find the relationship between the tool geometry and the cutting force or power.

In Chapter 3, the contact mechanics are presented to introduce the stress distribution in pure elastic deformation region. Since the shape of the contact objects influence the stress distribution and the location of first yield, the contact of a rigid sphere and a deformable flat surface, as well as a rigid cone and a deformable flat are investigated respectively. The maximum shear stress and von Mises stress locate below the contact area for spherical contact, which means that the point of first yield is hidden beneath the surface. The fracture is from inside of specimen to the contact surface. In contrast, for rigid conical contact the maximum shear stress and von Mises stress locate at the contact surface, thus the fracture starts from the surface to inside of specimen. Since, the location of first fracture is preferred on the surface for removing material efficiently for a cutting tool, the conical shape is selected as the basic geometry of a cutting tool. In addition, the stress distribution is affected by the cone angle, that is the cone angle increases the stress decreases.

When plastic strains are large compared to the elastic strains for rigid conical contact, the slip-line theory is simply discussed and the conical tool is moving as a "cutting tool" at a constant velocity. The mean contact pressure is used to estimate the von Mises yield stress and also related to the cone angle. Thus based on the material elastic, plastic and fracture process analysis, the cutting tool geometry effects the cutting force for material removal such that the smaller cutting tool angle, the smaller cutting force required for material fracture.

In addition, the orthogonal cutting mechanics is discussed too. The model developed by De Vries was presented. The rake angle is one key parameter influencing the required cutting force such that the cutting force decreases as the rake angle is increasing, or the tool angle is decreasing, which is same as the conclusion from the contact mechanism theory.

However, the cutting process is complicated and there is limitation of using simple analytical method to explain the entire cutting process, thus finite element analysis is used.

6.2.2 Cutting tool geometry 2D finite element analysis

The finite element analysis procedure and results are discussed in Chapter 4. Since biological sample has a complicated structure and mechanical properties, which could not be defined and analyzed for cutting analysis in Abaqus, a linear elastic and linear plastic

material model is defined for the cutting process analysis. For cutting tool computer-aided design, the rake angle of cutting tool is researched in 2D finite element analysis. The cutting model uses a splitting line, where the shear failure criterion is defined, for chip separation. The mesh element is CPS4R, which is a 4-node bilinear plane stress quadrilateral, reduced integration, hourglass control element type. The specimen is deformable and the cutting tool is a rigid body. According to the finite element analysis results, as the rake angle is increasing or the cutting tool angle is decreasing, the magnitude of cutting force is decreasing for achieving required von Mises criterion for material fracture.

The finite element analysis results coincides with the analytical analysis by using contact mechanics theory that a smaller magnitude of cutting force is achieved by a cutting tool with a smaller tool angle.

In addition, the finite element analysis results of different rake angle models also coincide with the analytical results by using cutting mechanics theory.

6.2.3 Preliminary biological sample cutting experiments

For finding the characteristic of real biological sample cutting, a preliminary biological sample cutting experiment is conducted in Chapter 5. Torque coil is used for the power or rotation transmission. The proximal tip of the torque coil is connected to a motor, and the distal end is connected to a cutter. The torque transducer between the torque

coil and the cutter is used to record the cutting torque. "Event" presents the instant when the cutting tool contacts the sample. Before the 'Event' the torque is the motor torque. After the "Event", the torque is increasing due to the increment of the contact between the cutting tool and the sample. Based on the previous analytical analysis and finite element analysis, for finding the influence of the cutting tool angle on the cutting force, two cutters are tested. The outer diameter are both 2.6mm and inner diameter are 2.0mm. The height of the cutting window is 4.0mm, and the width of the cutting window is 2.0mm. The difference is that the cutting angle is 90° and 55°, respectively. The test is running at rotation speed of 3000 rpm.

And the experiment result shows that as the cutting tool angle decreases, the magnitude of cutting force decreases, which is same as the analytical result and the finite element analysis result.

Therefore, based on the analytical analysis, finite element analysis, and experimental result, the decrement of the cutting tool angle can cause the decrement of the magnitude of cutting force.

7. Future work

The finite element analysis and experiments are required to be optimized. Current finite element analysis is based on a material model with linear elastic and linear plastic properties, which is not appropriate. Thus, the experiments for testing the biological sample material properties should be conducted. The elastic properties, plastic stress-strain response, fracture criterion should be found during the tests. The 2D finite element analysis should be optimized based on the biological material properties.

Based on the orthogonal cutting model, the cutting force is affected by the depth of cut and the width of cut. However, in 2D finite element analysis, the width of cut is not considered, so a 3D finite element analysis should be conducted. In addition, in preliminary cutting experiment, two types of cutting tools are tested with different shape of cutting edges, which possibly has influence on the cutting performance. Thus, the 3D finite element analysis for finding the influence of the cutting edges shape should be conducted. In addition, the preliminary biological sample cutting experiments need to be updated with mechanisms to monitor the cutting depth and cutting width. It is also suggested that the cutting forces are recorded as a function of the rotating angle of the cutting tool, and the whole process should be recorded by high speed camera. Thus, the response of the biological sample deformation to the cutting forces can be much clearly observed, which may be a benefit to reveal the biological sample deformation and fracture responses to different cutting conditions.

8. References

Abaqus, 27 May 2013, *Abaqus analysis theory and user's manual*, Version 6.12.

ASAHI INTECC, 28 May 2013, *Torque coil*, http://www.asahi-intecc.com/industrial/product/torque_coil.html, ASAHI INTECC.

Chanthasopeephan, T., Desal, J. P., and Lau, A. C.W., 2003, "Measuring forces in liver cutting: new equipment and experimental results," *Annals of Biomedical Engineering*, 31:1372-1382.

Cotton, P. B., 2008*Advanced Digestive Endoscopy: Practice and Safety*, Blackwell Publishing.

Covidien, *Directional Atherectomy*, 28 May 2013, http://www.ev3.net/peripheral/us/plaque-excision/, COVIDIEN.

De Vries, W. R., 1991, *Analysis of material removal process*, Springer-Verlag, New York.

EndoJaw, 27 May 2013, *Disposable Biopsy Forceps*, http://olympusamerica.com/msg_section/ET/files/F1004SB.pdf, Olympus.

Enteroscopy, 26 May 2013, *Injector Force Max Injection Needles*, http://www.olympusamerica.com/msg_section/ET/files/F1294SE.pdf, Olympus.

Ernst, H., and Merchant, M.E., 1941, "Chip formation, friction, and high quality machined surfaces," *Surface Treatment of Metals, Transactions of the American Society of Metals*, 29:299-378.

EZ Shot2, 26 May 2013, *Single use aspiration needle NA-220H/230H*, http://www.olympusamerica.com/msg_section/ET/files/EZShot2Brochure.pdf, Olympus.

Foreign body retrieval, 26 May 2013, *Olympus retrieval devices*, http://www.olympusamerica.com/msg_section/ET/files/RDPOSTER.pdf, Olympus.

Fay, J. A., 1998, *Introduction to fluid mechanics*, Massachusetts Institute of Technology Press.

Fischer-Cripps, C., 2007, *Introduction to Contact Mechanics*, Springer-Verlag, New York.

Fujinon, *Fujinon Endoscopy*, 26 May 2013, http://www.fujifilm.com/, Fujinon.

Fung, Y.C., 1993, *Biomechanics: Mechanical Properties of Living Tissues*, Springer-Verlag, New York, 2nd edition.

Gao, L. M., Chen, Y., and Lin, L.M., 1998, "Micro motor based on a new type of endoscope," *Proceeding of the 20th Annual International Conference of the IEEE Engineering in Medicine and Biology Society*, 20, No4.

Hemostasis Products, 27 May 2013, *QuickClip 2*, http://olympusamerica.com/msg_section/ET/files/F1142SB.pdf, Olympus,.

Hertz, H., 1881, "On the contact of elastic solids," *J. Reine Angew. Math*, 92:156-171. Translated and reprinted in English in *Hertz's Miscellaneous Papers*, Macmillan& Co., London, Ch5, 1896.

Hill, R., Lee, E.H. and Tupper, S.J., 1947, "Theory of wedge-indentation of ductile metals," *Proc. R. Soc. London, Ser.*, A188:273-289.

Huber, M.T., 1904, "Zur theorier der beruhrung fester elastischer korper," *Ann. Phys.*, 43:153-163.

Johnson, K. L., 2003, *Contact mechanics*, Cambridge University Press.

Lawn, B. R., Wilshaw, T.R., and Hartley, N. E. W., 1974, "A computer simulation study of hertzian cone crack growth," *Int. J. Fract.*, 10:1-16.

Lee, E.H., and Shaffer, B.W., 1951, "The theory of plasticity applied to a problem of machining," *ASME Transactions, Journal of Applied Mechanics*, 73:405-413.

Nachemson, AL. and Evans, JH., 1968 " Some mechanical properties of the third human interlaminar ligament (ligamentum favum)," *J Biomech* ., 1:211-216.

Namiki, 26 May 2013, *Namiki endoscopes*, http://www.namiki.net/, Namiki.

National Cancer Institute, 25 May 2013, *Definition*, http://www.cancer.gov/dictionary?CdrID=45882, National Cancer Institute.

Olympus, 26 May 2013, *Olympus endoscopes*, http://www.olympus-global.com/en, Olympus.

Pentax, 26 May 2013, *Pentax endoscopes*, http://www.pentaxmedical.com, Pentax .

Richard Dennis National Energy Technology Laboratory, 1992, *Fossil Energy Program*, http://fossil.energy.gov/programs/powersystems/turbines/turbines_howitworks.html U.S. Department of Energy.

Sneddon, I. N., 1948, "Boussinesq's problem for a rigid cone," *Proc. Cambridge Phil*os. *Soc.*, 44:492-507.

Water turbine, 24 May 2013, http://en.wikipedia.org/wiki/Water_turbine, Wikipedia.

Wildi, T., 2005, *Electrical Machines, Drives and Power Systems*, Sperika Enterprises Ltd..

Zhang, D.J., Liu, G., Sun, X., and Chen, M., 2008, "On saw-tooth chip formation in high speed cutting GH4169[J] ," *App. Mech. Mtl.*, 10:359–363.